JᴹM PAPERS

Energy pathways for large- and small-scale magnetic field generation in convection-driven plane layer dynamos

Souvik Naskar[1,2] 🄳 **and Anikesh Pal**[1] 🄳

[1]Department of Mechanical Engineering, Indian Institute of Technology, Kanpur 208016, India
[2]School of Earth and Environment, University of Leeds, Leeds LS2 9JT, UK
Corresponding author: Souvik Naskar, s.naskar@leeds.ac.uk

We use direct numerical simulations to investigate the energy pathways between the velocity and the magnetic fields in a rotating plane layer dynamo driven by Rayleigh–Bénard convection. The kinetic and magnetic energies are divided into mean and turbulent components to study the production, transport and dissipation in large- and small-scale dynamos. This energy balance-based characterisation reveals distinct mechanisms for large- and small-scale magnetic field generation in dynamos, depending on the nature of the velocity field and the conditions imposed at the boundaries. The efficiency of a dynamo in converting the kinetic energy to magnetic energy, apart from the energy redistribution inside the domain, is found to depend on the kinematic and magnetic boundary conditions. In a small-scale dynamo with a turbulent velocity field, the turbulent kinetic energy converts to turbulent magnetic energy via small-scale magnetic field stretching. This term also represents the amplification of the turbulent magnetic energy due to work done by stretching the small-scale magnetic field lines owing to fluctuating velocity gradients. The stretching of the large-scale magnetic field plays a significant role in this energy conversion in a large-scale turbulent dynamo, leading to a broad range of energetic scales in the magnetic field compared with a small-scale dynamo. This large-scale magnetic field stretching becomes the dominant mechanism of magnetic energy generation in a weakly nonlinear dynamo. We also find that, in the weakly nonlinear dynamo, an upscale energy transfer from the small-scale magnetic field to the large-scale magnetic field occurs owing to the presence of a gradient of the mean magnetic field.

Key words: geostrophic turbulence, dynamo theory, MHD turbulence

1007 A74-1

S. Naskar and A. Pal

1. Introduction

Hydromagnetic dynamo action is the commonly accepted source of magnetic fields in planets and stars. In this dynamo mechanism, a small magnetic perturbation can be amplified by the convective motion of an electrically conducting by electromagnetic induction. This dynamical process of electromagnetic induction involves the stretching and twisting of magnetic field lines by chaotic motions of the fluid, leading to the amplification of the field. This electromagnetic induction must overcome the Joule dissipation of the magnetic field by continuously converting the kinetic energy of the fluid to magnetic energy to sustain the dynamo action. A simple model of such dynamos is the Rayleigh–Bénard convection (RBC) in a plane layer between two parallel plates, heated from the bottom and cooled from the top, permeated by a magnetic field. Such plane layer convection of electrically conducting fluids was shown to induce dynamo action in early analytical (Childress & Soward 1972; Soward 1974; Fautrelle & Childress 1982) and numerical studies (Meneguzzi & Pouquet 1989).

The dynamics of flow and heat transfer in a plane layer RBC-driven dynamo depends on four governing non-dimensional numbers: (i) the Rayleigh number (Ra) representing the thermal forcing, (ii) the Ekman number(E) signifying the ratio of viscous force to Coriolis force, (iii) the thermal Prandtl number (Pr) and (iv) the magnetic Prandtl number (Pm); Pr and Pm are fluid properties as defined later in § 2.1. One of the most important diagnostic quantities is the magnetic Reynolds number (Rm), characterising the dominance of electromagnetic induction over ohmic diffusion of the magnetic field. These governing parameters decide the scale and strength of the generated magnetic field.

Dynamos are often classified based on the scale of the magnetic field generated by them (Brandenburg & Subramanian 2005). The magnetic field length scale is larger than the velocity length scale for a large-scale dynamo. Conversely, the magnetic field length scale is smaller than the velocity length scale for a small-scale dynamo. Celestial bodies, such as the Earth, generate global-scale magnetic fields driven by strongly turbulent small-scale convective motions. A plane layer may be viewed as a local approximation to the astrophysically more relevant spherical geometry. Owing to the relative simplicity of such a system, the mechanism of large-scale field generation in-plane layer convection-driven dynamos has been studied extensively in the literature. The inclusion of global rotation in such flows can break the reflectional symmetry of the convection to induce large-scale magnetic fields (Moffatt & Dormy 2019; Tobias 2021). In mean-field electrodynamics, where the statistical properties of the small-scale motion are related to the evolution of mean field by some transport coefficients, the α-effect characterises this symmetry-breaking. The α effect can be related to the kinetic helicity of the convective flow, which promotes large-scale field generation (Hughes 2018). The kinetic helicity in a plane layer rotating convection is high near the onset of convection (at $Ra = Ra_c$, where the critical Rayleigh number for the onset of convection scales as $Ra_c \sim O(E^{-4/3})$). However, despite the helical nature of the turbulence, Cattaneo & Hughes (2006) found no evidence of large-scale dynamo in their simulations. Moreover, in the rapidly rotating regime, where the flow is both vigorously turbulent and rotationally constrained, the kinetic helicity is found to be small (Tilgner 2012). This paradox leads to concerns about the applicability of the mean-field electrodynamics theory for plane layer rapidly rotating convection. Therefore, the mechanism for large-scale magnetic field generation in the rapidly rotating regime remains controversial in the literature, as reviewed in the next few paragraphs.

Stellmach & Hansen (2004) used the plane layer set-up to study weakly nonlinear dynamo convection at $E = 10^{-4} - 5 \times 10^{-7}$ with a low degree of supercriticality, $\mathcal{R} = Ra/Ra_c = 1.178$. They found that the magnetic field varies alternately between low- and high-intensity levels at $E = 5 \times 10^{-7}$ with small-scale structures dominating the flow field at low magnetic field intensity. These small-scale organised helical structures can efficiently convert kinetic energy to magnetic energy, leading to a large-scale velocity field with a large magnetic field intensity. However, the large-scale velocity field is relatively unorganised and inefficient for energy conversion. Therefore, the magnetic energy intensity falls again, leading to the breakdown of small-scale motions. This cyclic process leads to a highly time-dependent flow structure and magnetic field in their simulations. However, while such weakly nonlinear convection may drive a large-scale dynamo, only small-scale dynamo action without any significant α-effect has been reported by Cattaneo & Hughes (2006). In rapidly rotating compressible convection, Käpylä *et al.* (2009) demonstrated the existence of large-scale dynamos at modestly supercritical Ra, although the presence of a stratified layer in their simulations complicates the interpretation (Favier & Bushby 2013). However, driving a large-scale dynamo becomes progressively difficult further from the onset of convection, with only small-scale dynamos prevailing in the turbulent regime (Favier & Bushby 2013).

For a plane layer dynamo, the classification between small- and large-scale field generation becomes apparent from the fraction of energy in the mean magnetic field to the total magnetic energy (Tilgner 2012). The magnetic Reynolds number at the convective scale $\widetilde{Rm} = Rm\,E^{1/3}$, representing the dominance of electromagnetic induction over ohmic diffusion at the small convective scales, is one of the important diagnostic quantities that decides this mean energy fraction. In the study by (Tilgner 2012), large-scale dynamos with high mean energy fraction, $O(0.1)$, have been found to operate at low magnetic Reynolds numbers $\widetilde{Rm} \lesssim 13$. Higher values of $\widetilde{Rm}$ lead to a transition to small-scale magnetic field generation with a comparatively lower mean energy fraction. The kinetic helicity is high and nearly constant below the transition and then decreases rapidly with the increasing turbulence after the transition. Therefore, before the transition, kinetic helicity was proposed to be the driving mechanism of a large-scale dynamo, whereas the small-scale magnetic field generation after the transition is driven by the stretching of magnetic field lines by the velocity field. Similar transitions between large- and small-scale dynamo action can also be found for rotating compressible convection simulations of Käpylä *et al.* (2009); Favier & Bushby (2013), as noted by Guervilly, Hughes & Jones (2015).

Rapidly rotating convection in the regime of geostrophic turbulence can lead to the formation of large-scale vortices (Guervilly, Hughes & Jones 2014) that provide another possible means of large-scale magnetic field generation. These large-scale vortices occur for sufficiently rapid rotation ($Ro_c \lesssim 0.1$, where $Ro_c = E(Ra/Pr)^{1/2}$ is the convective Rossby number) and high turbulence $\widetilde{Ra} = RaE^{4/3} > 20$. These vortices form due to an upscale energy transfer in rotating turbulence and have been studied by Favier, Silvers & Proctor (2014). In particular, a non-local cascade of energy from the small scales towards the large scales takes place in addition to the regular forward cascade associated with the stretching of small-scale baroclinic vortices. The three-dimensional mode associated with small-scale baroclinic vortices follows the classical inertial scaling of $k^{-5/3}$ (where k is the wavenumber), corresponding to a three-dimensional forward energy cascade. In contrast, the two-dimensional mode associated with the large-scale vortex motion exhibits a k^{-3} scaling, consistent with a direct enstrophy cascade. The convection planform is dominated by a large horizontal-scale barotropic vortex, which is invariant in the direction of rotation. Nearly all the kinetic energy is concentrated in this two-dimensional mode. However,

the underlying small-scale baroclinic convective vortices remain qualitatively unchanged while continuously feeding the large-scale mode. Guervilly *et al.* (2015) demonstrated the generation of the magnetic field by these large-scale vortices in a plane layer dynamo convection. However, the generated magnetic field was strong enough to suppress the large-scale vortex that led to its formation. This magnetic field becomes weak to allow the large-scale vortex to grow again, leading to a cyclic variation between large- and small-scale velocity and magnetic fields.

Introducing a large-scale shear flow in small-scale rotating convection provides another avenue for large-scale magnetic field generation (Hughes & Proctor 2009). Hughes & Proctor (2013) studied the effect of a large-scale uni-directional horizontal shear flow in the plane layer model of Cattaneo & Hughes (2006). The interactions between the small-scale convection and large-scale shear lead to significant energy in large-scale magnetic fields, apart from a broader spectrum of energetic scales in the magnetic field. Here, the dynamo process is found to be dependent on all the scales in the flow field without any evidence of scale separation.

Another hint for a large-scale magnetic field generation is given using the asymptotic theory by Calkins *et al.* (2015) and Calkins (2018). An increase in magnetic diffusivity in strongly turbulent small-scale convection (i.e. with low helicity) has been shown to promote large-scale magnetic field generation for $\widetilde{Rm} \sim O(E^{1/6})$. Recent direct numerical simulations by Yan & Calkins (2022*b*) confirm this estimate. In their simulations, large-scale 'energetically robust' dynamos are produced that approach a mean energy fraction of unity with $\widetilde{Rm} \lesssim O(1)$. Therefore, these observations raise a possibility of a large-scale dynamo driven by rapidly rotating turbulent convection with small helicity.

The discussion in the above paragraphs reveals that, although many researchers extensively explored the mechanism of large-scale magnetic field generation from small-scale convective motions, there is no quantitative framework to compare them. The novelty of this study is to utilise an energy-based approach to investigate the proposed mechanisms of large- and small-scale magnetic field generation. Our analysis distinguishes between the part of the kinetic energy that produces the horizontally averaged large-scale mean magnetic field and the small-scale turbulent magnetic field. Based on this decomposition, we derive the kinetic and magnetic energy budgets and characterise dynamos with both large- and small-scale magnetic fields based on their energy conversion mechanisms. The energy budget equations consist of various energy exchange terms between large- and small-scale velocity and magnetic fields that provide a robust framework for understanding the large- and small-scale field generation. The production of magnetic energy by small-scale magnetic field stretching is found to be the dominant mechanism for small-scale field generation. A significant large-scale field can be produced by increasing magnetic diffusivity, giving rise to a broad range of energetic scales in a large-scale dynamo with a turbulent velocity field. An upscale energy transfer from the small-scale magnetic field, producing a large-scale magnetic field was found to be the dominant mechanism for magnetic field generation in a weakly nonlinear dynamo. The boundary conditions imposed at the walls are found to decide the redistribution of energy inside the control volume. We present the governing equations with the boundary conditions in § 2.1 and the budget equations for the kinetic and magnetic energies in § 2.2. We have performed direct numerical simulations of four dynamos to demonstrate the vertical profiles of the budget terms. The details of the simulations and the rationale for the choice of parameters are presented in §§ 2.3 and 3.1. In §§ 3.2 and 3.3, we present our findings on the kinetic and magnetic energy balances of these dynamos, respectively, and summarise our findings in § 4.

2. Method

2.1. *Governing equations*

In this study, the plane layer dynamo is driven by a classical RBC set-up with a plane layer of incompressible, electrically conducting, Boussinesq fluid kept between two parallel plates with a distance d and temperature difference ΔT, where the lower plate is hotter than the upper plate. The system rotates with a constant angular velocity Ω about the vertical axis, anti-parallel to the gravity g. This fluid has the density ρ, kinematic viscosity ν, thermal diffusivity κ, adiabatic volume expansion coefficient α, magnetic permeability μ, electrical conductivity σ and magnetic diffusivity η. The governing equations are non-dimensionalised with the distance between the plates d as the length scale, the free-fall velocity $u_f = \sqrt{(g\alpha\Delta T)d}$ as the velocity scale and $\sqrt{\rho\mu}u_f$ as the scale of the magnetic field. The Navier–Stokes equations, coupled with the energy equation, the induction equation and the solenoidal field conditions, govern the velocity, pressure, temperature and the magnetic field $\{u_i, p, \theta, B_i\}$ as presented below

$$\frac{\partial u_j}{\partial x_j} = \frac{\partial B_j}{\partial x_j} = 0, \tag{2.1}$$

$$\frac{\partial u_i}{\partial t} + u_j\frac{\partial u_i}{\partial x_j} = -\frac{\partial p}{\partial x_i} + \frac{1}{E}\sqrt{\frac{Pr}{Ra}}\epsilon_{ij3}u_j\hat{e}_3 + B_j\frac{\partial B_i}{\partial x_j} + \theta\delta_{i3} + \sqrt{\frac{Pr}{Ra}}\frac{\partial^2 u_i}{\partial x_j\partial x_j}, \tag{2.2}$$

$$\frac{\partial \theta}{\partial t} + u_j\frac{\partial \theta}{\partial x_j} = \frac{1}{\sqrt{RaPr}}\frac{\partial^2 \theta}{\partial x_j\partial x_j}, \tag{2.3}$$

$$\frac{\partial B_i}{\partial t} + u_j\frac{\partial B_i}{\partial x_j} = B_j\frac{\partial u_i}{\partial x_j} + \sqrt{\frac{Pr}{Ra}}\frac{1}{Pm}\frac{\partial^2 B_i}{\partial x_j\partial x_j}. \tag{2.4}$$

The governing non-dimensional parameters are the Rayleigh number ($Ra = g\alpha\Delta T d^3/\kappa\nu$) and the Ekman number ($E = \nu/2\Omega d^2$) representing the thermal forcing and rotation rates, respectively. The thermal and magnetic Prandtl numbers ($Pr = \nu/\kappa$ and $Pm = \nu/\eta$) are the properties of the fluid. The current set-up is a local approximation to the astrophysically more relevant spherical shell dynamo models (Tilgner 2012). In the horizontal directions (x_1, x_2) periodic boundary conditions are applied. We use no-slip and free-slip boundary conditions in the vertical direction (x_3)

$$u_1 = u_2 = u_3 = 0 \text{ at } x_3 = \pm 1/2 \qquad \text{(no slip)}$$

$$\frac{\partial u_1}{\partial x_3} = \frac{\partial u_2}{\partial x_3} = 0, \ u_3 = 0 \text{ at } x_3 = \pm 1/2 \qquad \text{(free slip)}. \tag{2.5}$$

Thermal boundary conditions are isothermal with unstable temperature gradients

$$\theta = 1/2 \text{ at } x_3 = -1/2, \quad \theta = -1/2 \text{ at } x_3 = 1/2. \tag{2.6}$$

Perfectly conducting and pseudo-vacuum boundary conditions have been used for the magnetic field

$$\frac{\partial B_1}{\partial x_3} = \frac{\partial B_2}{\partial x_3} = B_3 = 0 \text{ at } x_3 = \pm 1/2 \qquad \text{(perfectly conducting)},$$

$$B_1 = B_2 = \frac{\partial B_3}{\partial x_3} = 0 \text{ at } x_3 = \pm 1/2 \qquad \text{(pseudo-vacuum)}. \tag{2.7}$$

2.2. *Energy budget*

We perform a Reynolds decomposition of the variables into mean and fluctuating parts such that $\phi(x, y, z, t) = \overline{\phi}(z, t) + \phi'(x, y, z, t)$ where $\phi = \{u_i, p, \theta, B_i\}$. Here, the overbar denotes an average over the horizontal directions. The kinetic energy($K = 1/2u_i u_i$) and magnetic energy ($M = 1/2 B_i B_i$) are also divided into the mean ($\mathfrak{K}$ and $\mathfrak{M}$) and turbulent ($\mathcal{K}$ and $\mathcal{M}$) components, and are presented in (2.12)–(2.22). This decomposition into mean and turbulent parts of the energies is the primary distinctive feature of the present study from an earlier budget analysis of a dynamo (Brandenburg *et al*. 1996). We can derive these equations in three steps as follows:

(i) Firstly, (2.2) and (2.4) are horizontally averaged to get the mean momentum and mean induction equations, respectively,

$$\frac{\partial \overline{u_i}}{\partial t} + \frac{\partial}{\partial x_j}(\overline{u_i u_j} + \overline{u_i' u_j'}) = -\frac{\partial \overline{p}}{\partial x_i} + \frac{1}{E}\sqrt{\frac{Pr}{Ra}}\epsilon_{ij3}\overline{u_j}\hat{e}_3 + \frac{\partial}{\partial x_j}(\overline{B_i B_j} + \overline{B_i' B_j'})$$
$$+ \overline{\theta}\delta_{i3} + \sqrt{\frac{Pr}{Ra}}\frac{\partial^2 \overline{u_i}}{\partial x_j \partial x_j}, \tag{2.8}$$

$$\frac{\partial \overline{B_i}}{\partial t} + \frac{\partial}{\partial x_j}(\overline{u_j}\overline{B_i} + \overline{u_j' B_i'}) = \frac{\partial}{\partial x_j}(\overline{u_i}\overline{B_j} + \overline{u_i' B_j'}) + \sqrt{\frac{Pr}{Ra}}\frac{1}{Pm}\frac{\partial^2 \overline{B_i}}{\partial x_j \partial x_j}. \tag{2.9}$$

These mean equations (2.8) and (2.9) can be subtracted from (2.2) and (2.4), respectively, to get the fluctuating parts of the momentum and the induction equations as expressed below

$$\frac{\partial u_i'}{\partial t} + \frac{\partial}{\partial x_j}(u_i'\overline{u_j} + \overline{u_i}u_j' + u_i'u_j' - \overline{u_i'u_j'}) = -\frac{\partial p'}{\partial x_i} + \frac{1}{E}\sqrt{\frac{Pr}{Ra}}\epsilon_{ij3}u_j'\hat{e}_3$$
$$+ \frac{\partial}{\partial x_j}(B_i'\overline{B_j} + \overline{B_i}B_j' + B_i'B_j' - \overline{B_i'B_j'}) + \theta'\delta_{i3} + \sqrt{\frac{Pr}{Ra}}\frac{\partial^2 u_i'}{\partial x_j \partial x_j}, \tag{2.10}$$

$$\frac{\partial B_i'}{\partial t} + \frac{\partial}{\partial x_j}(\overline{u_j}B_i' + u_j'\overline{B_i} + u_j'B_i' - \overline{u_j'B_i'})$$
$$= \frac{\partial}{\partial x_j}(\overline{u_i}B_j' + u_i'\overline{B_j} + u_i'B_j' - \overline{u_i'B_j'}) + \sqrt{\frac{Pr}{Ra}}\frac{1}{Pm}\frac{\partial^2 B_i'}{\partial x_j \partial x_j}. \tag{2.11}$$

(ii) We multiply the mean velocity and mean magnetic field with the mean momentum equation (2.8) and the mean induction equation (2.9) respectively to get the evolution equations for $\mathfrak{K}$ and $\mathfrak{M}$.

(iii) Finally, the fluctuating velocity and magnetic fields can be multiplied with fluctuating parts of momentum and induction equations (2.10) and (2.11) respectively, and averaging them to get evolution equations for $\mathcal{K}$ and $\mathcal{M}$.

2.2.1. *Kinetic energy budgets*
Following the above steps, the turbulent kinetic energy (TKE) evolves as

$$\frac{\mathrm{d}\mathcal{K}}{\mathrm{d}t} = \mathcal{S} + \mathcal{B} - \mathcal{D} - \frac{\partial \mathcal{T}_j}{\partial x_j} + \mathcal{P}, \tag{2.12}$$

where

$$\mathcal{K} = \frac{1}{2}\overline{u_i' u_i'}, \tag{2.13a}$$

$$\mathcal{S} = -\overline{u_i' u_j'}\frac{\partial \overline{u_i}}{\partial x_j}, \tag{2.13b}$$

$$\mathcal{B} = \overline{u_3' \theta'}, \tag{2.13c}$$

$$\mathcal{D} = \sqrt{\frac{Pr}{Ra}}\,\overline{\frac{\partial u_i'}{\partial x_j}\frac{\partial u_i'}{\partial x_j}}. \tag{2.13d}$$

Here, $\mathcal{K}$ is the TKE, $\mathcal{S}$ is the production of TKE due to work done by the Reynolds stress $-\overline{u_i' u_j'}$ on the mean strain rate $\partial \overline{u_i}/\partial x_j$, $\mathcal{B}$ is the conversion of available potential energy (APE) to TKE by the turbulent buoyancy flux (Gayen, Hughes & Griffiths 2013), $\mathcal{D}$ is the viscous dissipation which converts TKE to internal energy (IE). Additionally, the redistribution of TKE is expressed as $\partial \mathcal{T}_j/\partial x_j$, representing the divergence of the TKE flux $\mathcal{T}_j$, which can be further divided into the following components:

$$\mathcal{T}_p = \overline{u_j' p'}, \tag{2.14a}$$

$$\mathcal{T}_t = \frac{1}{2}\overline{u_i' u_i' u_j'}, \tag{2.14b}$$

$$\mathcal{T}_v = -\sqrt{\frac{Pr}{Ra}}\frac{\partial \mathcal{K}}{\partial x_j}, \tag{2.14c}$$

$$\mathcal{T}_M = -\overline{B_j}\,\overline{u_i' B_i'} - \overline{u_i' B_i' B_j'}, \tag{2.14d}$$

$$\mathcal{T}_j = \mathcal{T}_p + \mathcal{T}_t + \mathcal{T}_v + \mathcal{T}_M. \tag{2.14e}$$

The components of the TKE flux are the pressure flux, $\mathcal{T}_p$, the turbulent flux $\mathcal{T}_t$, the viscous flux $\mathcal{T}_v$ and the magnetic flux $\mathcal{T}_M$, representing the redistribution of $\mathcal{K}$ by the fluctuating pressure field, velocity field, viscous diffusion and the magnetic field. Among the two terms in (2.14d), the first term indicates a contribution from the mean magnetic field.

In (2.12), the term $\mathcal{P}$ represents the production of TKE due to work done by the Lorentz force on the flow field. It can be further divided into three components, as shown below

$$\mathcal{P}_1 = \overline{B}_j B_i' \frac{\partial u_i'}{\partial x_j}, \tag{2.15a}$$

$$\mathcal{P}_2 = \overline{u_i' B_j'}\frac{\partial \overline{B}_i}{\partial x_j}, \tag{2.15b}$$

$$\mathcal{P}_3 = \overline{B_i' B_j'\frac{\partial u_i'}{\partial x_j}}, \tag{2.15c}$$

$$\mathcal{P} = -\mathcal{P}_1 + \mathcal{P}_2 - \mathcal{P}_3. \tag{2.15d}$$

Among these three terms, $\mathcal{P}_1$ is the production of turbulent magnetic energy from TKE due to work done by the fluctuating strain rate, $\partial u_i'/\partial x_j$, on the mean magnetic field, $\mathcal{P}_2$ signifies the production of magnetic energy from TKE in the presence of a mean magnetic field gradient $\partial \overline{B}_i/\partial x_j$ and $\mathcal{P}_3$ represents the amplification of the magnetic energy, due

to work done by stretching of small-scale magnetic field lines by the fluctuating velocity gradients.

The mean kinetic energy (MKE) budget can be expressed as

$$\frac{\mathrm{d}\mathfrak{K}}{\mathrm{d}t} = -\mathcal{S} + \mathfrak{B} - \mathfrak{D} - \frac{\partial \mathfrak{T}_j}{\partial x_j} + \mathfrak{P}, \tag{2.16}$$

where

$$\mathfrak{K} = \frac{1}{2}\overline{u}_i \overline{u}_i, \tag{2.17a}$$

$$\mathfrak{B} = \overline{u}_3 \overline{\theta}, \tag{2.17b}$$

$$\mathfrak{D} = \sqrt{\frac{Pr}{Ra}} \frac{\partial \overline{u}_i}{\partial x_j} \frac{\partial \overline{u}_i}{\partial x_j}, \tag{2.17c}$$

$$\mathfrak{T}_j = \overline{u_j}\ \overline{p} + \frac{1}{2}\overline{u_i' u_j'}\overline{u}_i - \sqrt{\frac{Pr}{Ra}} \frac{\partial \mathfrak{K}}{\partial x_j} - \overline{B_i' B_j'}\overline{u}_i - \overline{B}_i\ \overline{B}_j \overline{u}_i. \tag{2.17d}$$

Here, $\mathfrak{K}$ is the MKE, $\mathfrak{B}$ is the mean buoyancy flux, $\mathfrak{D}$ is the mean viscous dissipation and $\partial \mathfrak{T}_j / \partial x_j$ is the divergence of the MKE flux $\mathfrak{T}_j$. Additionally, the exchange of energy with magnetic field $\mathfrak{P}$ can be further divided into the following components:

$$\mathcal{P}_4 = \overline{B_i' B_j'} \frac{\partial \overline{u}_i}{\partial x_j}, \tag{2.18a}$$

$$\mathcal{P}_5 = \overline{B}_i\ \overline{B}_j \frac{\partial \overline{u}_i}{\partial x_j}, \tag{2.18b}$$

$$\mathfrak{P} = -\mathcal{P}_4 - \mathcal{P}_5. \tag{2.18c}$$

In the above equations, $\mathcal{P}_4$ represents the work done by the magnetic stress $\overline{B_i' B_j'}$ on the mean strain rate $\partial \overline{u}_i / \partial x_j$, similar to the shear production term $\mathcal{S}$ in (2.13b). The work done by the mean magnetic field in the presence of mean shear $\partial \overline{u}_i / \partial x_j$ is represented by $\mathcal{P}_5$.

2.2.2. *Magnetic energy budgets*

Now, we look into the evolution equations for the turbulent and the mean magnetic energies. The induction equation (2.4) is similar to the vorticity transport equation, where we define vorticity as the curl of the velocity field $\omega_i = \epsilon_{ijk}\partial \omega_k / \partial x_j$. Similarly, the magnetic energy equations resemble enstrophy transport equations (Lumley & Tennekes 1997). The turbulent magnetic energy (TME) budget equation is given below

$$\frac{\mathrm{d}\mathcal{M}}{\mathrm{d}t} = -\mathcal{D}^M - \frac{\partial \mathcal{T}_j^M}{\partial x_j} + \mathcal{P}^M, \tag{2.19}$$

where

$$\mathcal{M} = \frac{1}{2}\overline{B_i' B_i'}, \tag{2.20a}$$

$$\mathcal{D}^M = \frac{1}{Pm}\sqrt{\frac{Pr}{Ra}} \frac{\overline{\partial B_i'}}{\partial x_j} \frac{\partial B_i'}{\partial x_j}, \tag{2.20b}$$

$$\mathcal{T}_j^M = \frac{1}{2}\overline{B_i' B_i' u_j'} - \frac{1}{Pm}\sqrt{\frac{Pr}{Ra}} \frac{\partial \mathcal{M}}{\partial x_j}. \tag{2.20c}$$

Here, $\mathcal{M}$ is the TME, $\mathcal{D}^M$ is the Joule dissipation of TME, $\partial \mathcal{T}_j^M / \partial x_j$ is the redistribution of TME flux $\mathcal{T}_j^M$. In (2.20c) the two terms signify the redistribution of TME by the velocity field and ohmic diffusion, respectively.

Furthermore, the exchange of energy with the velocity and mean magnetic field is represented by $\mathcal{P}^M$ as defined below

$$\mathcal{P}_6 = \overline{u_j' B_i'} \frac{\partial \overline{B}_i}{\partial x_j}, \tag{2.21a}$$

$$\mathcal{P}^M = \mathcal{P}_1 + \mathcal{P}_3 + \mathcal{P}_4 - \mathcal{P}_6. \tag{2.21b}$$

Here, $\mathcal{P}_6$ represents the energy exchange between the turbulent and mean magnetic fields. We can anticipate its appearance in the mean magnetic energy (MME) equations with an opposite sign

$$\frac{d\mathfrak{M}}{dt} = -\mathfrak{D}^M - \frac{\partial \mathfrak{T}_j^M}{\partial x_j} + \mathfrak{P}^M. \tag{2.22}$$

In the above equation

$$\mathfrak{M} = \frac{1}{2} \overline{B}_i \overline{B}_i, \tag{2.23a}$$

$$\mathfrak{D}^M = \frac{1}{Pm} \sqrt{\frac{Pr}{Ra}} \frac{\partial \overline{B}_i}{\partial x_j} \frac{\partial \overline{B}_i}{\partial x_j}, \tag{2.23b}$$

$$\mathfrak{T}_j^M = \overline{B}_i \overline{u_j' B_i'} - \overline{B}_i \overline{u_i' B_j'} - \frac{1}{Pm} \sqrt{\frac{Pr}{Ra}} \frac{\partial \mathfrak{M}}{\partial x_j}, \tag{2.23c}$$

where $\mathfrak{M}$ is the MME, $\mathfrak{D}^M$ is the mean Joule dissipation and $\partial \mathfrak{T}_j^M / \partial x_j$ is the divergence of MME flux $\mathfrak{T}_j^M$. Energy exchange terms in the MME equation can be decomposed as,

$$\mathfrak{P}^M = -\mathcal{P}_2 + \mathcal{P}_5 + \mathcal{P}_6. \tag{2.24}$$

A consolidated pictorial view of the equations with colour coding is shown in figure 1 to enhance readability.

2.2.3. *Volume-avergaed energy budgets*

We plot an energy pathway diagram by vertically averaging the terms in the energy budget equations to obtain the volume-averaged quantities, as shown in figure 2. The energy transport terms, coloured in grey in figure 1, become negligible due to this volume averaging. The motivation here is to demonstrate the conversion paths between kinetic energy and magnetic energy sustaining the dynamo action. The APE, at the top of this diagram, is converted to MKE and TKE via the mean and turbulent parts of the buoyancy flux, $\langle \mathfrak{B} \rangle$ and $\langle \mathcal{B} \rangle$, respectively (Gayen *et al.* 2013). The shear production term, $\mathcal{S}$, may also produce TKE in the presence of a mean shear. The small-scale turbulent flow can exchange energy with the small-scale magnetic field through $\mathcal{P}_1$ or $\mathcal{P}_3$ or both, or with the large-scale mean magnetic field through $\mathcal{P}_2$. The large-scale flow can exchange energy with the small-scale and large-scale magnetic fields through $\mathcal{P}_4$ and $\mathcal{P}_5$, respectively. The term $\mathcal{P}_6$ may produce TME by extracting energy from the mean magnetic field. It may also produce MME by transferring energy from the turbulent magnetic field to the mean magnetic field. Finally, the viscous dissipation components ($\mathfrak{D}$ and $\mathcal{D}$) convert the kinetic energy to IE, while the magnetic energy transforms to IE via Joule dissipation
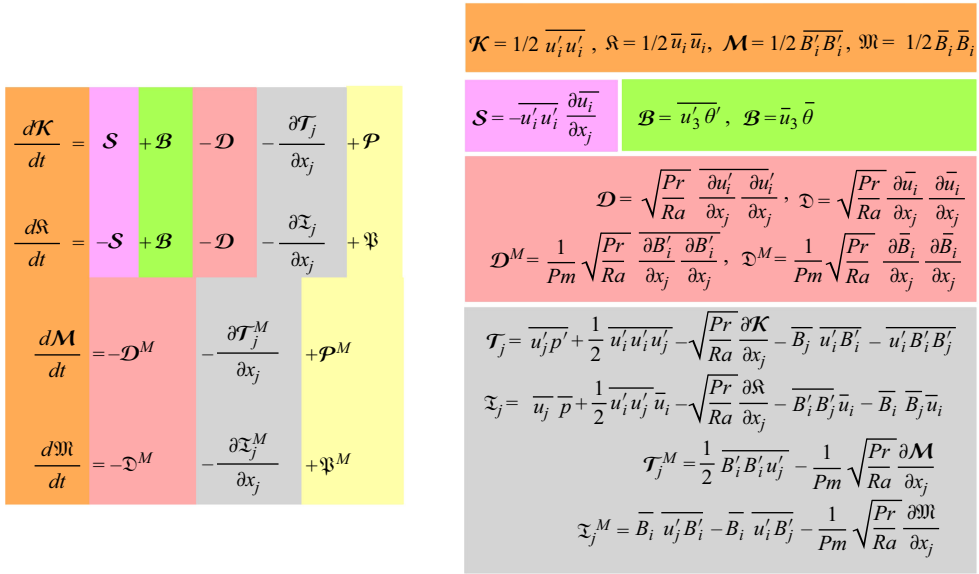
Figure 1. Consolidated view of the budget equations. The TKE, MKE, TME and MME equations are shown in the left column. The corresponding expressions for the terms are colour coded in the right column.
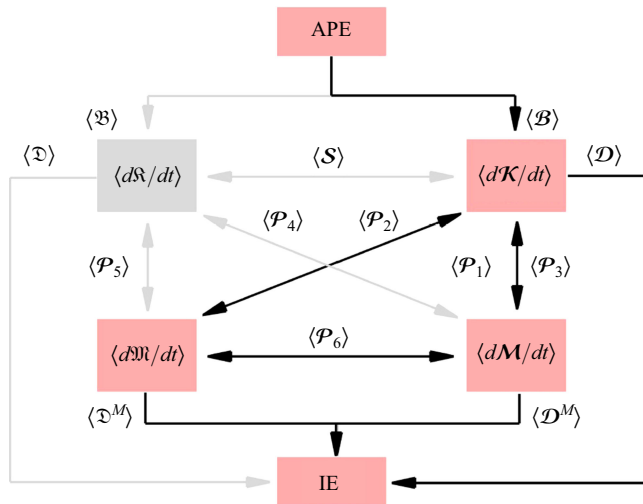

Figure 2. Energy pathways between the kinetic and magnetic energies in a convection-driven dynamo. The energetic terms shown here are volume averaged as indicated by angular brackets $\langle . \rangle$. The energy pathways marked in grey are negligible in the absence of a mean flow.

components ($\mathfrak{D}^M$ and $\mathcal{D}^M$). In the absence of a horizontally averaged mean velocity field, as in the present problem, the energy pathways associated with MKE, marked in grey, are insignificant.

2.3. *Numerical details*

We perform direct numerical simulations of RBC-driven dynamos to characterise the different types of dynamos based on the energy pathway diagram in figure 2. The

Journal of Fluid Mechanics

	Re_0	Nu_0	Rm	Nu	Re	Λ	ER
Stellmach & Hansen (2004)	48.3	1.34	170.7	1.66	68.3	0.38	1.37
Validation study	48.6	1.36	168.5	1.68	67.4	0.36	1.36

Table 1. Results from the three test runs to reproduce results from rotating non-magnetic convection and rotating dynamo simulations of Stellmach & Hansen (2004). Subscript $'0'$ represents non-magnetic rotating convection. The Elasser numbers and the magnetic to kinetic energy ratio are represented by Λ and ER, respectively.

governing equations are solved using the finite difference method (Bakhuis *et al.* 2018) in a staggered grid arrangement. The scalar quantities (pressure and temperature) are stored at the cell centres, whereas the velocity and the magnetic field components are stored at the cell faces. We use a second-order central difference scheme for spatial discretisation. The projection method is used to calculate the divergence-free velocity field where the pressure Poisson equation is solved using a parallel multigrid algorithm. Similarly, an elliptic divergence cleaning algorithm is employed to keep the magnetic field solenoidal (Brackbill & Barnes 1980). An explicit third-order Runge–Kutta method is used for time advancement except for the diffusion terms, which are solved implicitly using the Crank–Nicolson method (Pham, Sarkar & Brucker 2009; Brucker & Sarkar 2010). The computational domain is a doubly periodic cube of unit aspect ratio. This domain is approximately 26 times larger than the critical horizontal wavelength at the onset of rotating convection ($\lambda_c = 4.8158E^{1/3}$) (Chandrasekhar 1961). Therefore, we can ensure the statistical convergence of all the diagnostic properties (Yan & Calkins 2022a) presented in tables 2 and 3. We use 1024 uniform grids in each horizontal direction (x_1 and x_2) and 256 grids in the vertical direction (x_3) with clustering near the boundaries to resolve the boundary layers. This choice of grid ensures that the grid spacing does not exceed a factor of $2-4$ times the local Kolmogorov length scale (Brucker & Sarkar 2010), signifying sufficient resolution to calculate the second-order moments and resolve all the length scales in the simulations. The spectra of kinetic and magnetic energies (see figure 4) demonstrate sufficient resolution for all our simulations. Furthermore, the deviation from the overall balance of energy is shown in table 3. This indicates the difference between buoyant power input and the total dissipation (viscous and magnetic), which remains less than 5 %, demonstrating sufficient resolution in all the simulations.

Validation of our numerical solver is performed by replicating the results from rotating convection simulations of Stellmach & Hansen (2004) at $Ra = 1.4 \times 10^7$, $E = 10^{-6}$ and $Pr = 1$, along with their rotating dynamo convection simulation results for $Pr_m = 2.5$ with free-slip boundary conditions. Our results are in good agreement with this study, as demonstrated in table 1. The details of the validation studies, grid resolution and boundary layer resolution tests for the same parameters in rotating RBC-driven dynamos are given in Naskar & Pal (2022a,b). Apart from these, the solver has been validated extensively for studies on non-magnetic rotating stratified flow and various transitional and turbulent shear flows (Pal, de Stadler & Sarkar 2013; Pal & Sarkar 2015; Pal 2020; Pal & Chalamalla 2020; Singh & Pal 2023, 2024a,b).

3. Results and discussion

We compare the energy conversion pathways for four dynamos with diagnostic quantities enlisted in table 2. From our previous simulations (Naskar & Pal 2022b), we choose two dynamo cases at $\mathcal{R} = Ra/Ra_c = 10$, $Pr = 1$ and $Pm = 1$, where Ra_c is the Rayleigh

case	$\mathcal{R}$	Pm	Ro_C	$\widetilde{Ra}$	$\widetilde{Rm}$	$\langle\mathfrak{M}\rangle/M$	$\widetilde{H}$	Nu	type
R10Pm1N	10	1	0.069	76.0	33.4	0.0006	0.21	55.0	small
R10Pm1F	10	1	0.074	87.0	27.6	0.0011	0.29	64.7	small
R10Pm0.1F	10	0.1	0.074	87.0	3.2	0.2811	0.23	60.7	large
R2Pm0.2N	2	0.2	0.031	15.2	1.5	0.6129	9.51	8.5	large

Table 2. Volume-averaged diagnostic quantities for the dynamo simulations at $E = 5 \times 10^{-7}$ and $Pr = 1$. The last column indicates the dynamo types.

case	$\langle\mathcal{P}_1\rangle$	$-\langle\mathcal{P}_2\rangle$	$\langle\mathcal{P}_3\rangle$	$-\langle\mathcal{P}_6\rangle$	$\langle\mathcal{D}\rangle$	$\langle\mathcal{D}^M\rangle$	$\langle\mathfrak{D}^M\rangle$	balance(%)	type
R10Pm1N	0.0002	0.0000	0.3491	0.0000	0.6232	0.3507	0.0000	2.7	small
R10Pm1F	0.0004	0.0014	0.7549	0.0013	0.1827	0.7812	0.0001	3.7	small
R10Pm0.1F	0.1397	0.0093	0.5696	0.0069	0.2457	0.7289	0.0026	3.6	large
R2Pm0.2N	0.3399	0.0068	0.0538	−0.0055	0.6252	0.3518	0.0120	3.3	large

Table 3. Volume-averaged energy exchange rates and dissipation for the dynamo simulations at $E = 5 \times 10^{-7}$ and $Pr = 1$. The balance indicates overall deviation from the balance of energy ($(\langle\mathcal{B}\rangle - \mathcal{D} - \mathcal{D}^M - \mathfrak{D}^M)/\langle\mathcal{B}\rangle) \times 100$ %. The last column indicates the dynamo types.

number at the onset of non-magnetic rotating convection at $E = 5 \times 10^{-7}$. At this Ekman number, the critical Rayleigh number $Ra_c = 3.830 \times 10^9$ for no-slip and $Ra_c = 2.192 \times 10^9$ for free-slip boundary conditions. We designate these two cases in table 2 as R10Pm1N and R10Pm1F. The case R10Pm1N is simulated using no slip and electrically conducting boundaries, whereas free slip and pseudo-vacuum boundaries (Naskar & Pal 2022b) are incorporated for the R10Pm1F case. The instantaneous snapshots of the magnetic field in the x_1-direction, as depicted in figures 3(a) and 3(b), illustrate the small-scale nature of the magnetic field produced by these turbulent dynamos.

We simulated another dynamo case with otherwise the same parameters as R10Pm1F, except lowering Pm to 0.1 as denoted by R10Pm0.1F in table 2. In this case, lowering Pm leads to large-scale magnetic field generation, as evident from figure 3(c). Additionally, we simulate a case with $\mathcal{R} = 2$ and $Pm = 0.2$ and designate it as R2Pm0.2N. This case is also a large-scale dynamo with weakly nonlinear convection (Stellmach & Hansen 2004) as demonstrated by the large-scale magnetic field in figure 3(d).

3.1. *Diagnostic quantities*

The volume-averaged diagnostic parameters reported in table 2 outline the global behaviour of these dynamos. The convective Rossby number, $Ro_C = E(Ra/Pr)^{1/2}$, representing the ratio of inertia to the Coriolis force, is of the order of 10^{-2}, indicating the dominant role of the Coriolis force. Therefore, all the dynamos are produced by rapidly rotating convection with comparatively small inertia (Naskar & Pal 2022b). The reduced Rayleigh number $\widetilde{Ra} = Ra E^{4/3}$ indicates that the dynamos operate in a turbulent state of the flow for $\mathcal{R} = 10$, whereas for $\mathcal{R} = 2$ weakly nonlinear columnar convection has been observed (Stellmach & Hansen 2004; Naskar & Pal 2022a).

Additionally, the reduced magnetic Reynolds number $\widetilde{Rm} = Rm E^{1/3}$ represents the strength of electromagnetic induction relative to ohmic diffusion at the convective scales. Large-scale dynamos are expected for $\widetilde{Rm} \lesssim O(1)$ (Yan & Calkins 2022b). The distinction between large- and small-scale dynamos (Tilgner 2012) is apparent from the mean energy
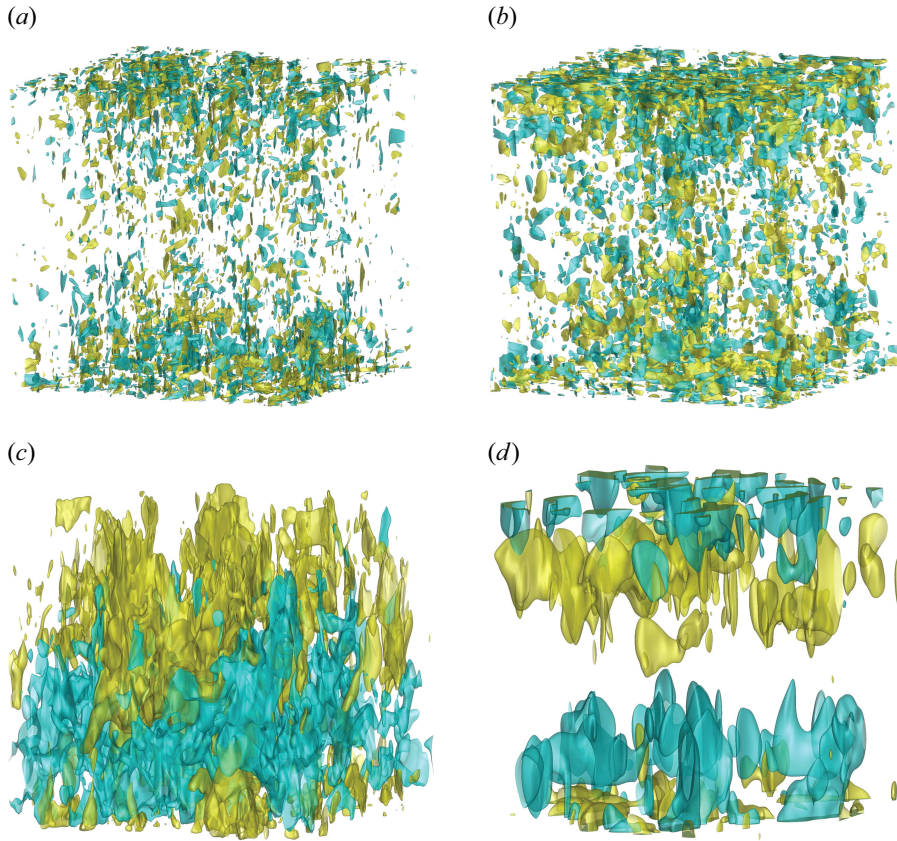
Figure 3. The structure of the magnetic field generated by the dynamos for the cases (*a*) R10Pm1F, (*b*) R10Pm1N, (*c*) R10Pm0.1F, (*d*) R2Pm0.2N as visualised by the isosurface $B_1 = \pm 0.03$ (olive, positive; blue, negative).

fraction $\langle \mathfrak{M} \rangle / M$, where $M = \langle \mathfrak{M} \rangle + \langle \mathcal{M} \rangle$. For the small-scale dynamos, the volume-averaged MME is three orders of magnitude smaller than the TME. However, they are of the same order for the large-scale dynamos. Kinetic helicity is another important quantity related to large-scale magnetic field generation from small-scale turbulence. Under the influence of rapid rotation, convection is helical (Vogt, Horn & Aurnou 2021), and this helicity can induce a large-scale magnetic field by stretching and twisting the magnetic field lines over the horizontal plane. We tabulate a scaled value of the kinetic helicity $\widetilde{H} = H E^{-1/3}$ to compare the values with (Tilgner 2012) (see figure 3 in his paper). Here, $H = \int h^2 \mathrm{d}x_3$ is a volume-averaged measure of the velocity–vorticity correlation defined as

$$h = \frac{\overline{u_i \omega_i}}{(\overline{u_j u_j})^{1/2} (\overline{\omega_k \omega_k})^{1/2}}. \tag{3.1}$$

The scaled helicity remains small for all other cases compared with R2Pm0.2N.

We can now discuss the rationale behind our choice of the cases. The velocity field of the small-scale dynamos, R10Pm1N and R10Pm1F, is turbulent enough to produce a small-scale magnetic field. Yet, the turbulence intensity is small enough to keep the inertial force small, as compared with the Coriolis force ($Ro_C \sim O(10^{-2})$). Therefore, they fulfil our purpose of studying a small-scale dynamo operating in the geophysically
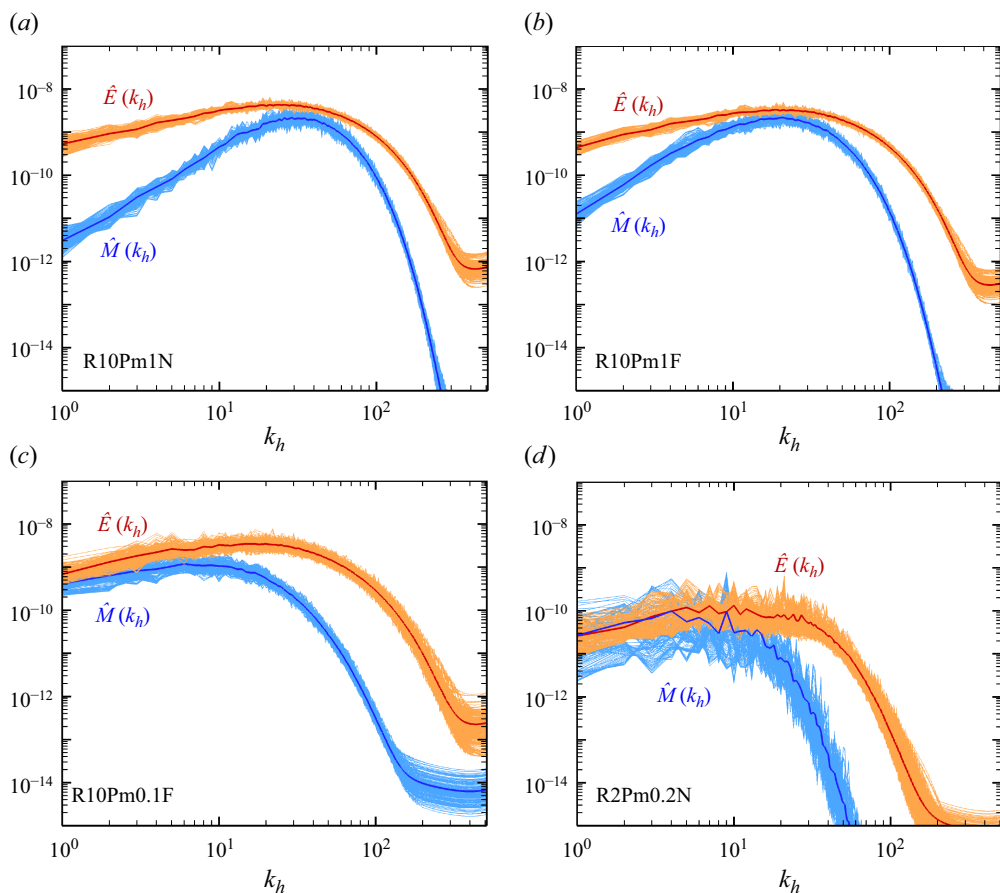
Figure 4. The spectral distribution of the kinetic energy ($\hat{E}$) and the magnetic energy ($\hat{M}$) in the horizontal wavenumbers ($k_h = \sqrt{k_x^2 + k_y^2}$) for the dynamos (*a*) R10Pm1F, (*b*) R10Pm1N, (*c*) R10Pm0.1F, (*d*) R2Pm0.2N). Instantaneous energy spectra (thin lines) have been averaged over the horizontal mid-plane. The corresponding time-averaged spectra have been overlapped with thick lines.

relevant rapidly rotating convective regime. These two cases differ only in the choice of boundary conditions but produce magnetic fields with distinct strengths and topologies (Naskar & Pal 2022*b*). Comparison of these two cases, therefore, allows us to isolate the effect of the boundary conditions on the energy conversion pathways.

The spectral energy distribution of total kinetic and magnetic energies ($\hat{E}$ and $\hat{M}$) for the dynamos R10Pm1N and R10Pm1F are presented in figures 4(*a*) and 4(*b*), respectively. For R10Pm1N, the kinetic energy peaks at $k_h = 23$, whereas the peak magnetic energy is at a larger but comparable wavenumber of $k_h = 29$. For R10Pm1F, the corresponding peaks for kinetic and magnetic energies are at $k_h = 19$ and $k_h = 21$, respectively. This indicates that the magnetic energy peaks at a smaller scale (i.e. higher wavenumber) than the velocity field. Additionally, the magnetic energy at the large scales (i.e. low wavenumbers) is much smaller than the kinetic energy at these scales, making the fraction of magnetic energy much smaller than the total energy. Therefore, we classify these two cases as small-scale dynamos.

Yan & Calkins (2022*a*) demonstrated the role of magnetic diffusion on large-scale magnetic field generation. Large-scale dynamos, with large mean energy fractions, were

shown to be found at $\widetilde{Rm} \lesssim O(1)$. Following their study, the case R10Pm0.1F has been simulated by starting from the statistically stationary solution of R10Pm1F and lowering the magnetic Prandtl number from $Pm = 1$ to $Pm = 0.1$ to achieve $\widetilde{Rm} \sim O(1)$. The spectral distribution of magnetic energy for R10Pm0.1F in figure 4(*c*) is significantly different from R10Pm1F in figure 4(*b*), although the kinetic energy distribution remains similar. In particular, we see an increase in the magnetic energy in the lower wavenumber with a peak at $k_h = 6$, compared with a peak kinetic energy at $k_h = 17$, indicating large-scale dynamo action.

Another large-scale dynamo, R2Pm0.2N, has been simulated following the study by Stellmach & Hansen (2004), who reported large-scale dynamo action when Ra was near the onset of non-magnetic rotating convection. Tilgner (2012) proposed kinetic helicity as the driving mechanism for the large-scale magnetic field in such a weakly supercritical velocity field. The spectral energy distribution for this case, as shown in figure 4(*d*), exhibits both large-scale velocity and magnetic fields with the peak energies at $k_h = 6$ and $k_h = 4$, respectively. We qualitatively compare the energy conversion mechanisms in the two large-scale dynamos, R10Pm0.1N and R2Pm0.2N. Notice that, for R2Pm0.2N, the rescaled helicity $\tilde{H} = 9.51$ is much higher as compared with that of R10Pm0.1F, for which the helicity has a similar value to the small-scale dynamos. This confirms the findings of Yan & Calkins (2022*a*) that enhanced magnetic diffusion may replace helicity as a mechanism for large-scale field generation in strongly turbulent flows. In the present study, we study the mechanism of large- and small-scale magnetic field generation in terms of energy pathways.

The large-scale dynamos also exhibit strongly time-dependent velocity and magnetic fields, as seen from the energy spectrum (see e.g. figure 4*d*). Similar time variability has been demonstrated in previous literature (Stellmach & Hansen 2004; Guervilly, Hughes & Jones 2017). Therefore, we present the time series of kinetic and magnetic energies for the large-scale dynamos, apart from the time variability of the energy budget terms for R2Pm0.2N. The time series of the volume-averaged mean and fluctuating energies ($\langle \mathfrak{M} \rangle$ and $\langle \mathcal{M} \rangle$), along with the mean energy fraction ($\langle \mathfrak{M}/M \rangle$), are presented for the two large-scale dynamos R10Pm0.1F and R2Pm0.2N in figures 5(*a*) and 5(*b*), respectively. Both dynamos exhibit significant time dependence. The mean magnetic field displays more time dependence for both dynamos than the fluctuating field. For R10Pm0.1F small time scale fluctuations can be observed owing to higher turbulence.

The vertical structure of the mean magnetic field is also illustrated for the two large-scale dynamos R10Pm0.1F and R2Pm0.2N in figures 6(*a*) and 6(*b*). The structure is similar to a spiral staircase with a twist in the anti-clockwise direction (i.e. same as the direction of rotation). The turbulent dynamo R10Pm0.1F exhibits a more complex antisymmetric vertical structure, than the weakly nonlinear dynamo R2Pm0.2N which has a symmetric structure similar to the dynamo reported by Stellmach & Hansen (2004), albeit at $Pm = 1$. For both cases, the staircase structure of the mean magnetic field rotates clockwise with a fixed periodicity similar to such dynamos reported in previous studies (Stellmach & Hansen 2004; Guervilly *et al.* 2017). It should be noted here that there is no vertical component of the mean magnetic field (i.e. $\overline{B}_3 = 0$) for the purely conducting magnetic boundary conditions used for R2Pm0.2N. Even for R10Pm0.1F, the vertical component of the field is negligibly small.

We have also demonstrated the time variability of the terms in the TKE, TME and MME budgets for R2Pm0.2N (figure 7 *a–c,* respectively), as the energy spectra (figure 4*d*) exhibits the strongest variability for this dynamo. Among the budget terms $\langle \mathcal{P}_2 \rangle$ and $\langle \mathcal{P}_6 \rangle$ exhibit strong time dependence. However, none of the terms change their sign over the
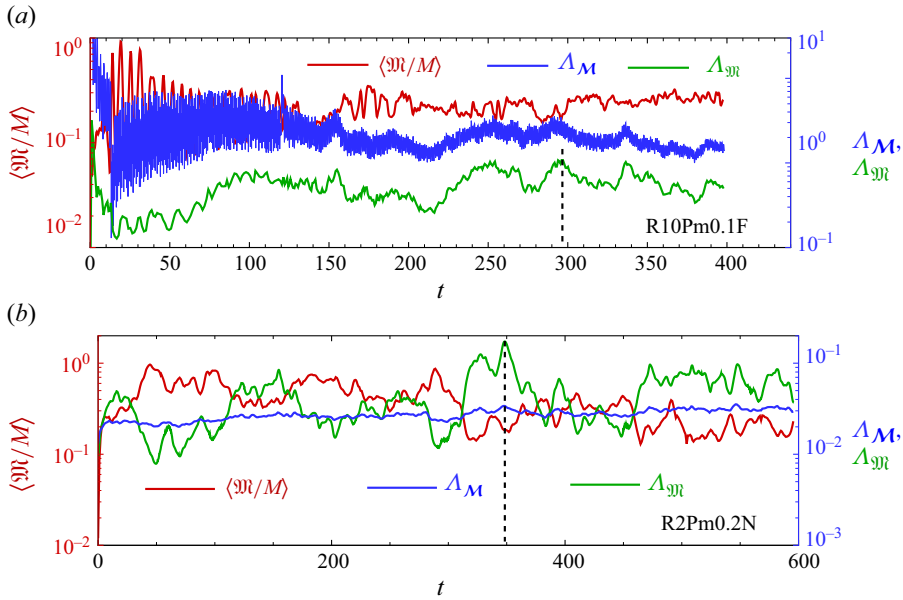
Figure 5. Time variation of the magnetic energies for (*a*) R10Pm0.1F and (*b*) R2Pm0.2N in free-fall time units. The *y*-axis on the left shows the energy ratio, while the energies are plotted on the right *y*-axis. The magnetic field strength is expressed in terms of Elsasser numbers defined as $\Lambda_{\mathcal{M}} = 2RaE\langle\mathcal{M}\rangle Pm/Pr$ and $\Lambda_{\mathfrak{M}} = 2RaE\langle\mathfrak{M}\rangle Pm/Pr$.
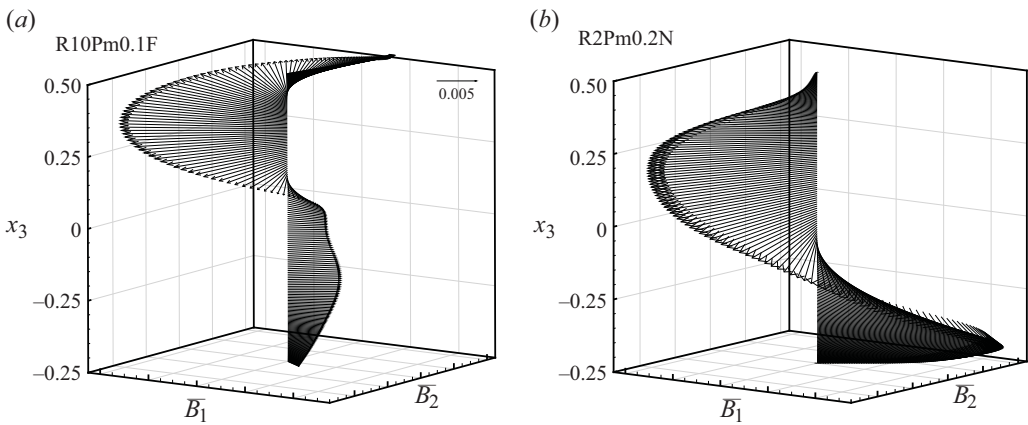

Figure 6. Snapshot of the vertical structure of the mean magnetic field at the time instants shown by the vertical dashed line in figure 5.

run time of the simulations for any of the dynamos studied here. Therefore, the direction of energy transfer (e.g. TKE to TME or TME to MME) as indicated by the sign of the volume and time averages of these quantities (see table 3) stays the same throughout the simulation run. However, individual scalar components of the energy exchange terms (e.g. $\mathcal{P}_3 = \mathcal{P}_3^{ij} = \overline{B_i' B_j' \partial u_i' / \partial x_j}$) can become positive or negative depending on the magnetic boundary conditions (Naskar & Pal 2022*b*).
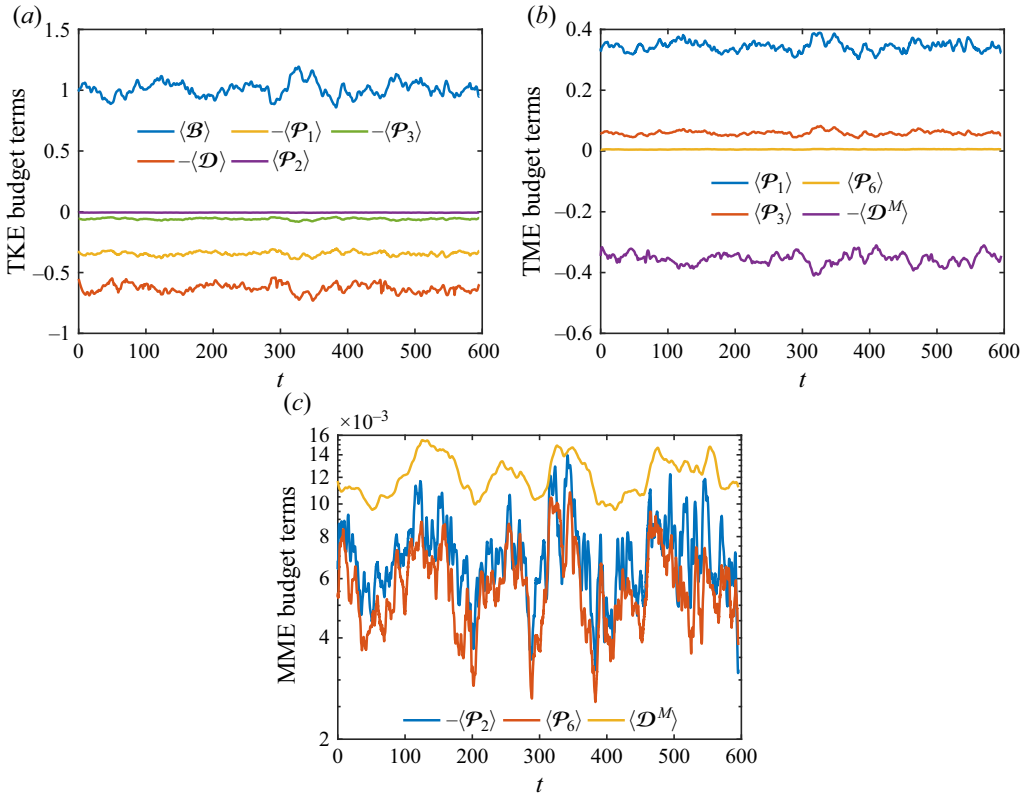
1007 A74-16

Figure 7. Time history of the terms in (*a*) TKE (*b*) TME and (*c*) MME budgets. The MME budget terms are plotted using a log scale as they exhibit strong time dependence.

3.2. *Kinetic energy budget*

Now we can look at the vertical variation of the horizontally averaged TKE terms in (2.12) for the four cases in figure 8. All the terms in this equation have been averaged over time and normalised by $(Ra\,Pr)^{1/2}/(Nu-1)$ in this figure. This makes the volume average of the source term ($\mathcal{B}$) to be unity (Kerr 2001). The Nusselt number $Nu = qd/k\Delta T$, where q is the total vertical heat flux, is a non-dimensional measure of convective heat transport through the fluid layer, as reported in table 2. There is a primary balance among the turbulent buoyancy flux ($\mathcal{B}$), TKE transport ($\partial \mathcal{T}_j/\partial x_j$), viscous dissipation ($\mathcal{D}$) and the conversion to magnetic energy ($\mathcal{P}$) for all the dynamos. For instance, in figure 8(*a*), the TKE is generated by $\mathcal{B}$ in the bulk, which is partly transported by $\partial \mathcal{T}_j/\partial x_j$ towards the boundaries where $\mathcal{D}$ dominates. The vertical variation of all the terms, except $\mathcal{P}$, are qualitatively similar with non-magnetic rotating convection (Kunnen, Geurts & Clercx 2009; Guzmán *et al.* 2020).

The variations of the various transport components are presented separately in figure 9 with the behaviour near the lower boundary demonstrated in the insets. Among the transport components in a non-rotating, non-magnetic RBC, the pressure transport ($\partial \mathcal{T}_P/\partial x_j$) is the primary mechanism that transfers TKE towards boundaries whereas the viscous transport ($\partial \mathcal{T}_v/\partial x_j$) is higher near the boundaries (figure 9*a*). A detailed analysis of the kinetic energy transport in such flows has been explored by Petschel *et al.* (2015). The different flux contributions in (2.14) dominate the TKE transport at different depths in the domain. Based on this, the domain can be separated into multiple layers with distinct
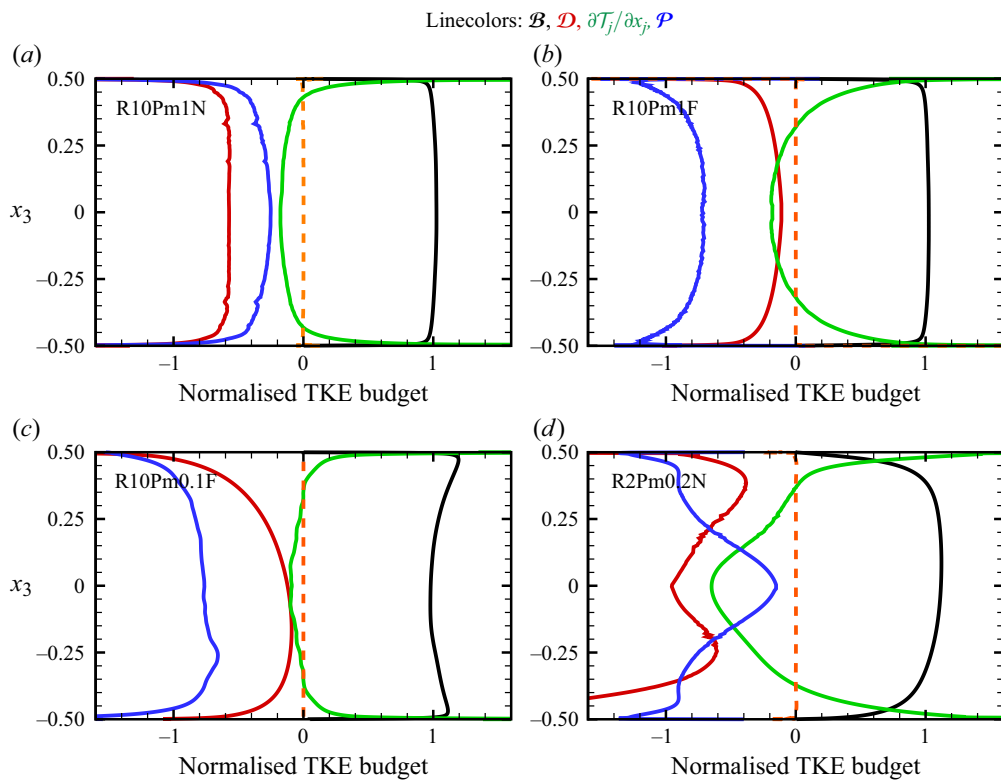
Linecolors: $\mathcal{B}$, $\mathcal{D}$, $\partial \mathcal{T}_j / \partial x_j$, $\mathcal{P}$

Figure 8. Vertical variation of the terms in TKE budget for the (*a*) R10Pm1N, (*b*) R10Pm1F, (*c*) R10Pm0.1F, (*d*) R2Pm0.2N cases. The orange dashed line indicates the balance as defined by the difference between the left- and right-hand sides of the TKE budget equation (2.12), which indicates sufficient accuracy of the present calculations.

balances between the production, transport components and dissipation of TKE. In the following discussion, we briefly explore the effects of dynamo action on the various TKE terms, including TKE transport.

The small-scale dynamos R10Pm1N and R10Pm1F in figures 8(*a*) and 8(*b*) differ only in the boundary conditions. The choice of a no-slip boundary condition in R10Pm1N results in an Ekman layer near the boundaries. Moreover, the perfectly conducting magnetic boundary condition constrains the magnetic field to be horizontal near the boundaries as compared with a vertical magnetic field at the boundaries for a pseudo-vacuum boundary condition in R10Pm1F (Naskar & Pal 2022*b*). For R10Pm1N, the amount of TKE converted to IE via $\mathcal{D}$ is higher than the production of magnetic energy ($\mathcal{P}$), whereas the latter is higher for R10Pm1F (see also table 3). This indicates a more efficient dynamo action for R10Pm1F compared with R10Pm1N, attributed to the effect of boundary conditions on the magnetic field generation. A more elaborate discussion to disentangle the effects of velocity and magnetic boundary conditions can be found in Appendix A.

The small-scale dynamos differ in the redistribution of TKE (figures 9*a* and 9*b*). The redistribution of TKE for R10Pm1N in figure 9(*a*) is qualitatively similar to non-magnetic RBC, with negligible contribution from the magnetic field $\partial \mathcal{T}_M / \partial x_j$. However, for R10Pm1F in figure 9(*b*), the transport by the magnetic field is significant with an opposite sign compared with the pressure transport. In this case, the magnetic flux $\mathcal{T}_M$ transports TKE towards the interior from the boundaries, mitigating the effect of

Linecolors: $\partial \mathcal{T}_j/\partial x_j$, $\partial \mathcal{T}_p/\partial x_j$, $\partial \mathcal{T}_t/\partial x_j$, $\partial \mathcal{T}_\nu/\partial x_j$, $\partial \mathcal{T}_M/\partial x_j$
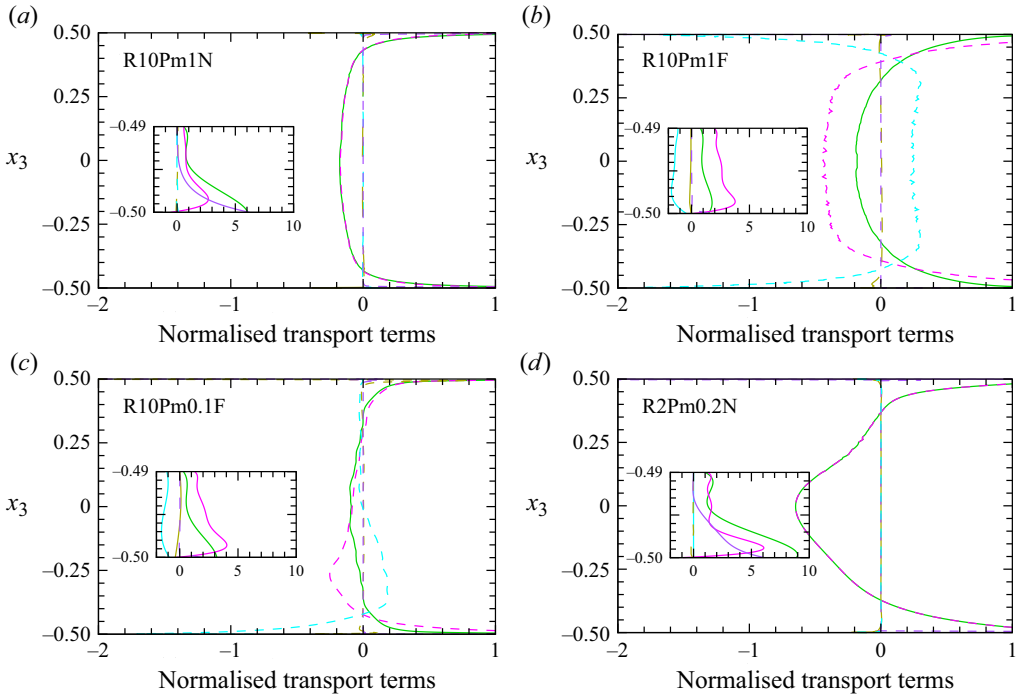

Figure 9. Vertical variation of the various components of the transport terms $\partial \mathcal{T}_j/\partial x_j$ in the TKE budget for the (*a*) R10Pm1N, (*b*) R10Pm1F, (*c*) R10Pm0.1F, (*d*) R2Pm0.2N cases. The insets show the variation of the transport terms near the bottom wall.

pressure transport. The difference in the behaviour of the magnetic flux is attributed to the difference in the vertical structure of the magnetic field owing to the difference in boundary conditions (Naskar & Pal 2022*b*). Although the TKE dissipation ($\mathcal{D}$) in the interior is significantly lower, as compared with R10Pm1N, the redistribution of TKE towards the boundaries, $\partial \mathcal{T}_j/\partial x_j$, remains similar in magnitude. The surplus TKE produced by $\mathcal{B}$ in the interior is balanced by the conversion to magnetic energy $\mathcal{P}$, which is significantly higher in R10Pm1F compared with R10Pm1N. For both cases, the magnetic flux $\mathcal{T}_M$ is dominated by the small-scale flux $\overline{u_i' B_i' B_j'}$ while the large-scale flux $\overline{B_j}\,\overline{u_i' B_i'}$ remains small. The viscous transport dominates the other transport terms near the boundaries for R10Pm1N. However, this term is small near the boundaries in R10Pm1F owing to the absence of an Ekman layer.

A comparison between the small-scale dynamo R10Pm1F and the large-scale dynamo R10Pm0.1F, in figures 8(*b*) and 8(*c*), does not show significant differences, except for the behaviour of the transport component, as shown in more detail in figures 9(*b*) and 9(*c*). The TKE transport $\partial \mathcal{T}_j/\partial x_j$ makes a much smaller contribution to the budget for the large-scale dynamo R10Pm0.1F as compared with the small-scale dynamo R10Pm1F. This indicates a spatially local conversion of TKE to TME and IE in R10Pm0.1F, while a comparatively higher redistribution of TKE in the bulk occurs in R10Pm1F. Among the two components of the magnetic energy flux in (2.14*d*), the contribution from the small-scale flux $\overline{u_i' B_i' B_j'}$ dominates in R10Pm1F, while the large-scale flux $\overline{B_j}\,\overline{u_i' B_i'}$ is significant for R10Pm0.1F.
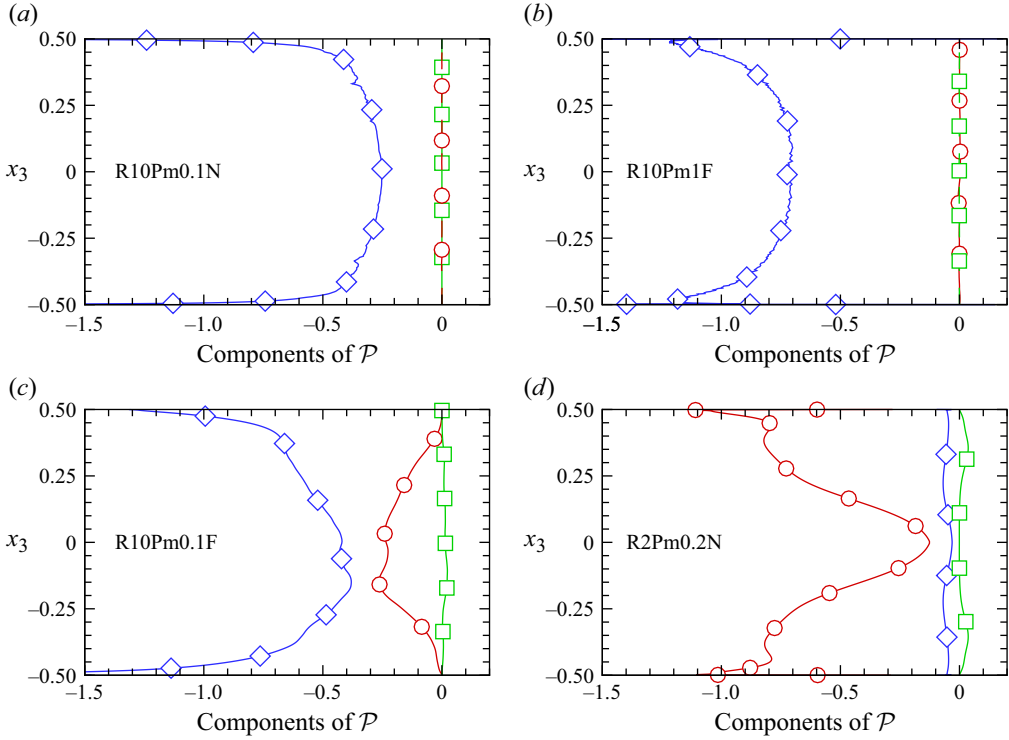
Figure 10. Components of the energy exchange term in TKE budget for (*a*) R10Pm1N, (*b*) R10Pm1F, (*c*) R10Pm0.1F and (*d*) R2Pm0.2N. The symbols denote $-\mathcal{P}_1$ (red, circles), $-\mathcal{P}_2$ (green, squares) and $-\mathcal{P}_3$ (blue, diamonds).

Additionally, we can contrast the TKE budget of a large-scale dynamo R10Pm0.1F against another large-scale dynamo with weakly nonlinear convection, R2Pm0.2N, in figures 8(*c*) and 8(*d*), where the transport terms can be contrasted in 9(*c*) and 9(*d*). It can be observed that the pressure transport term $\partial \mathcal{T}_P / \partial x_j$ dominates within the interior and redistributes energy towards the boundaries. The production of magnetic energy $\mathcal{P}$ exhibits more vertical dependence in this case (figure 8*d*) as compared with R10Pm0.1F (figure 8*c*). This should be due to the weaker turbulence in R2Pm0.2N that allows the development of a larger magnetic field gradient inside the domain.

Now we look into the individual contributions from the components of $\mathcal{P}$ in (2.15), as shown in figure 10. For the small-scale dynamos R10Pm1N and R10Pm1F in figures 10(*a*) and 10(*b*), the small-scale production of magnetic energy ($\mathcal{P}_3$) is the dominant component of $\mathcal{P}$. This term remains the dominant contributor to magnetic energy production for the large-scale dynamo R10Pm0.1F in figure 10(*c*), although the mean magnetic field plays an important role in converting TKE to TME through the term $\mathcal{P}_1$. This term is insignificant for the small-scale dynamos. For R2Pm0.2N in figure 10(*d*), the conversion of TKE to TME occurs through $\mathcal{P}_1$ while the small-scale production of TME, $\mathcal{P}_3$ remains small. Small values of $\mathcal{P}_2$ compared with the other terms in figures 10(*c*) and 10(*d*) reflect a much lower rate of conversion to MME compared with TME, as discussed in the next section.

3.3. *Magnetic energy budgets*

We now turn our attention to the magnetic energy budgets. The energy flow direction of each dynamo in figure 2 becomes apparent with the help of table 3. The terms $\mathcal{P}_1$ and $\mathcal{P}_3$
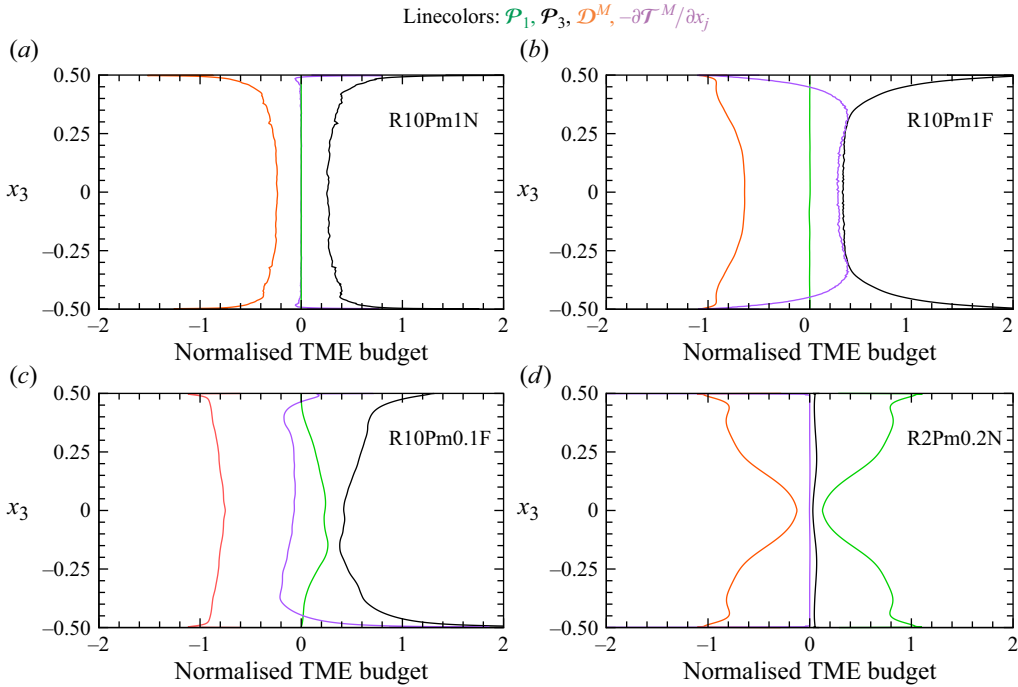
1007 A74-20

Figure 11. Vertical variation of the terms in TME budget for the (*a*) R10Pm1N, (*b*) R10Pm1F, (*c*) R10Pm0.1F, (*d*) R2Pm0.2N cases.

are positive, representing a conversion of TKE to TME by the action of a large-scale and a small-scale magnetic field, respectively. The term $\mathcal{P}_2$ is negative, indicating a generation of MME at the expense of TKE. The term $\mathcal{P}_6$ has negative values indicating a conversion of MME to generate TME, except for the case R2Pm0.2N, where the turbulent magnetic field provides energy to the mean magnetic field, exhibiting an upscale transfer of energy. However, $\mathcal{P}_2$ and $\mathcal{P}_6$ are small compared with the other terms in the budget, indicating a low energy exchange rate with the mean magnetic field.

We present the vertical profiles of the horizontally averaged TME terms in (2.19) in figure 11. In this budget equation, the exchange of energy with the velocity field ($\mathcal{P}_1$ and $\mathcal{P}_3$), and the large-scale magnetic field ($\mathcal{P}_6$) acts as the source of TME, whereas the Joule dissipation ($\mathcal{D}^M$) acts as a sink to convert TME to IE. In figure 11(*a*), the small-scale dynamo R10Pm1N has a primary balance between the small-scale production $\mathcal{P}_3$ and the Joule dissipation $\mathcal{D}^M$. Unlike R10Pm1N, the transport of TME $\partial \mathcal{T}_j^M / \partial x_j$ plays a significant role in the balance for R10Pm1F in figure 11(*b*) by redistributing the TME from the boundaries towards the interior of the domain. In contrast, the conversion from TME to IE by Joule dissipation is spatially local in R10Pm1N, without significant redistribution. However, volume-averaged TME balance for both small-scale dynamos reduces to the small-scale production of TME by stretching of magnetic field lines $\mathcal{P}_3$ and the ohmic dissipation, $\mathcal{D}^M$ as expressed below

$$\left\langle \overline{B_i' B_j' \frac{\partial u_i'}{\partial x_j}} \right\rangle \approx \frac{1}{Pm} \sqrt{\frac{Pr}{Ra}} \left\langle \overline{\frac{\partial B_i'}{\partial x_j} \frac{\partial B_i'}{\partial x_j}} \right\rangle. \tag{3.2}$$

This balance resembles small-scale enstrophy balance in a turbulent flow field. In such small-scale dynamos, the magnetic field stretches into filaments around the convective

vortices (Naskar & Pal 2022*b*), as represented by the term $\mathcal{P}_3$. The width of the filaments, representing the scale of the magnetic field, continuously decreases as they are stretched by the vortices until Joule dissipation ($\mathcal{D}^M$) takes over. The size of the vortices in strongly rotating convection scales as $E^{1/3}$. Therefore, the width of the filaments should be of the order of $E^{1/3}\widetilde{Rm}^{-1/2}$ (Tilgner 2012). As $\widetilde{Rm}$ is higher for R10Pm1N, it has a lower width of filaments, which results in a slightly higher wavenumber for the peak magnetic energy, as compared with R10Pm1F in figure 4. However, as $Pm = 1$, the magnetic field generates scales with the same order of magnitude as the velocity scale for both dynamos.

The TME balance for the large-scale dynamo R10Pm0.1F, as depicted in figure 11(*c*) is different from R10Pm1F in two aspects. Firstly, the $\mathcal{P}_1$ acts as a significant source of TME in R10Pm0.1F, unlike R10Pm1F, as already highlighted in figure 10. Note that the term $\mathcal{P}_1$ represents a similar mechanism of magnetic field generation as $\mathcal{P}_3$, with an additional presence of a mean field. The volume-averaged budget in R10Pm0.1F reduces to a balance between the total field stretching $\mathcal{P}_1 + \mathcal{P}_3$ and the Joule dissipation $\mathcal{D}^M$ as expressed below

$$\left\langle \overline{B_j}\, \overline{B'_i \frac{\partial u'_i}{\partial x_j}} \right\rangle + \left\langle \overline{B'_j B'_i \frac{\partial u'_i}{\partial x_j}} \right\rangle \equiv \left\langle \overline{B_j B'_i \frac{\partial u'_i}{\partial x_j}} \right\rangle \approx \frac{1}{Pm}\sqrt{\frac{Pr}{Ra}} \left\langle \overline{\frac{\partial B'_i}{\partial x_j} \frac{\partial B'_i}{\partial x_j}} \right\rangle. \qquad (3.3)$$

As the magnetic diffusivity increases (i.e. decrease in Pm), the ohmic diffusion allows larger magnetic field scales. The stretching of this large-scale field by the small-scale velocity gradients, $\mathcal{P}_1$, becomes an additional source of TME. Therefore, $\mathcal{P}_1$ implicitly represents the effect of magnetic diffusion on the TME budget. We note here that R10Pm0.1F is the only dynamo with significant TME production by both $\mathcal{P}_1$ and $\mathcal{P}_3$. Hence, it exhibits the broadest range of energetic scales in the magnetic energy spectrum in figure 4(*c*), compared with the other dynamos.

Another difference between R10Pm1F and R10Pm0.1F is present in the behaviour of the redistribution of TME. As shown in (2.20*c*), this term consists of the turbulent transport of TME by the turbulent velocity field $(1/2)\overline{B'_i B'_i u'_j}$, and the transport by ohmic diffusion $1/Pm\sqrt{Pr/Ra}\,\partial \mathcal{M}/\partial x_j$. For the small-scale dynamo R10Pm1F, the turbulent transport of TME dominates, whereas the diffusive transport dominates for R10Pm0.1F, owing to decreased Pm. This results in a change in the sign representing the direction of TME transport, as seen in figure 11(*c*). The individual contributions from the transport terms are not shown separately to improve the clarity of the figures.

The TME budget in the weakly supercritical dynamo R2Pm0.2N is primarily a balance between the large-scale magnetic field stretching $\mathcal{P}_1$ and Joule dissipation $\mathcal{D}^M$ as follows:

$$\left\langle \overline{B_j}\, \overline{B'_i \frac{\partial u'_i}{\partial x_j}} \right\rangle \approx \frac{1}{Pm}\sqrt{\frac{Pr}{Ra}} \left\langle \overline{\frac{\partial B'_i}{\partial x_j} \frac{\partial B'_i}{\partial x_j}} \right\rangle. \qquad (3.4)$$

As the turbulence is small, the contribution from small-scale magnetic field-stretching $\mathcal{P}_3$ remains small. For all four dynamos, the contribution to TME from MME ($\mathcal{P}_6$) remains much smaller in comparison with the other term and hence not shown in figure 11. Also, a perfectly conducting boundary condition suppresses the vertical redistribution of TME in R10Pm1N and R2Pm0.2N, unlike R10Pm1F and R10Pm0.1F, where there is significant redistribution of TME.

Finally, we look into the budget of the mean magnetic field in figure 12. The abscissas in these figures are differently scaled in proportion to the mean dissipation rate of the dynamos $\mathfrak{D}^M$, which is several orders of magnitude smaller compared with the turbulent dissipation, $\mathcal{D}^M$, for small-scale dynamos. For the large-scale dynamos R10Pm0.1 in
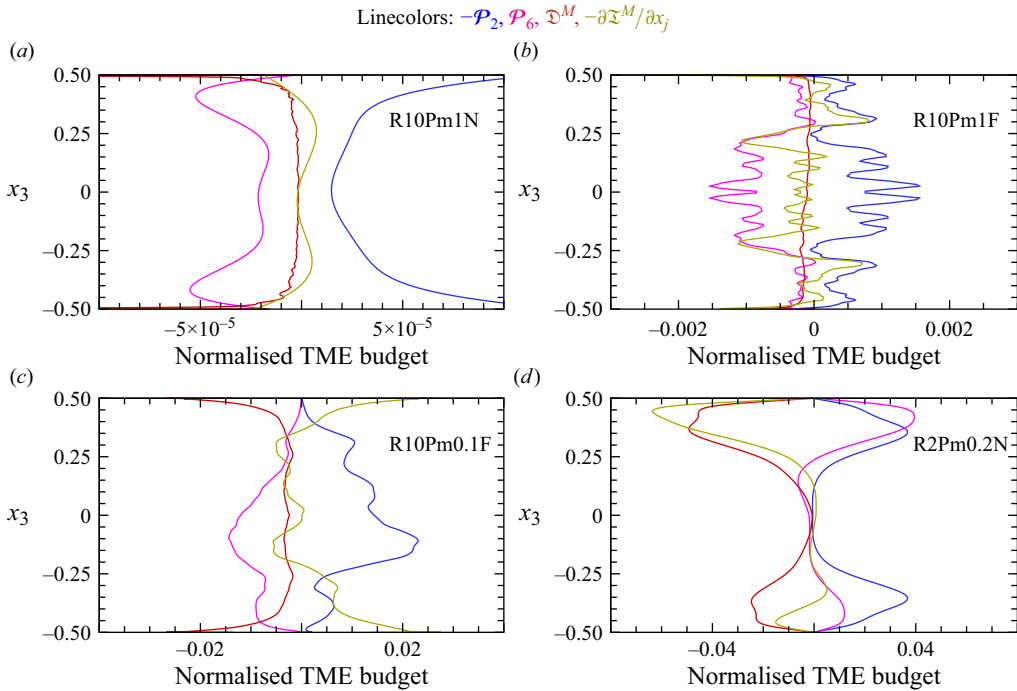
Linecolors: $-\boldsymbol{\mathcal{P}}_2$, $\boldsymbol{\mathcal{P}}_6$, $\mathfrak{D}^M$, $-\partial\mathfrak{T}^M/\partial x_j$

Figure 12. Vertical variation of the terms in the MME budget for the (*a*) R10Pm1N, (*b*) R10Pm1F, (*c*) R10Pm0.1F, (*d*) R2Pm0.2N cases.

figure 12(*c*), the mean dissipation increases by one order of magnitude compared with the small-scale dynamo R10Pm1F, owing to enhanced magnetic diffusion. In the MME budget, $\mathcal{P}_2$ is partially balanced by $\mathcal{P}_6$ in the interior. However, a part of the MME is transported towards the boundary and is converted to IE by the mean Joule dissipation $\mathfrak{D}^M$.

The large-scale dynamo in figure 12(*d*) demonstrates a transfer of TME to MME by $\mathcal{P}_6$ near the boundaries. This is the only dynamo where both the small-scale velocity and magnetic fields provide energy to the mean magnetic field through $\mathcal{P}_2$ and $\mathcal{P}_6$. The positive value of $\mathcal{P}_6$ represents an upscale energy transfer from TME to MME for this case. This upscale transfer of energy can be attributed to enhanced helicity of the flow for R2Pm0.2N, as shown in table 2. This enhanced supply of mean energy is balanced by enhanced mean Joule dissipation near the boundaries, whereas the magnetic energy terms are small near the midplane. The mean magnetic field in R10Pm0.1F primarily acts as a mediator, receiving energy from the velocity field and cascading towards a small-scale magnetic field, with much smaller mean Joule dissipation as compared with R2Pm0.2N. The ohmic diffusion term (the last term on the right-hand side of (2.23*c*)) dominates the transport of MME in R2Pm0.2N. In contrast, the first two terms in (2.23*c*) dominate the MME redistribution in R10Pm0.1F. We note here that a volume-averaged balance can be found between $\mathcal{P}_2$ and $\mathcal{P}_6$ as a source of MME and the mean dissipation $\mathfrak{D}^M$ as the sink of MME, from the values reported in table 3. The same balance can be derived from the balance between the electromotive force due to fluctuations and the large-scale diffusion in the mean induction equation, as demonstrated in Calkins *et al.* (2015).

4. Conclusions

The mechanism of large-scale magnetic field generation from small-scale motions in rapidly rotating turbulent convection remains a mystery to many researchers. According

to the mean-field electrodynamics theory, the α-effect, which is also related to kinetic helicity, results in a large-scale dynamo in rapidly rotating turbulent convection. However, the applicability of the mean-field theory in rapidly rotating turbulent convection remains controversial owing to the failure of rapidly rotating turbulent systems to act as large-scale dynamos despite the presence of helicity and small helicity for vigorously turbulent and rotationally constrained systems. Our present investigation attempts to provide a novel energy-based framework for understanding the various mechanisms of large-scale field generation reported in the literature. The kinetic and magnetic energy budgets in a plane layer convection-driven dynamo are decomposed into horizontally averaged mean and fluctuating components to distinguish between the energy exchange mechanisms operating at large and small scales. Based on this decomposition, we create an energy pathway diagram to study the energy exchange between the large- and small-scale velocity and the magnetic fields. We have performed direct numerical simulations of four dynamos to compare their energy pathways. Two of these dynamos, R10Pm1N and R10Pm1F, can be classified as small-scale dynamos with smaller MME fractions as compared with the other two large-scale dynamos, R10Pm0.1F and R2Pm0.2N. The small-scale dynamos also produce a magnetic field with a smaller scale compared with the velocity field, whereas R10Pm0.1F and R2Pm0.2N produce magnetic energy at larger scales comparable to the velocity field. This is evident from the spectral distribution of the kinetic energy and the magnetic energy in the horizontal wavenumber in figure 4.

The small-scale dynamos R10Pm1N and R10Pm1F differ by the relative magnitude of small-scale magnetic energy production $\mathcal{P}_3$ and viscous dissipation $\mathcal{D}$, with the latter being higher for R10Pm1N. This indicates comparatively efficient dynamo action with free-slip, pseudo-vacuum boundaries compared with a dynamo with no-slip, perfectly conducting boundaries. The redistribution of TKE inside the control volume also depends on the boundary conditions. Nevertheless, a balance between the magnetic energy production by small-scale magnetic field stretching ($\mathcal{P}_3$) and Joule dissipation, $\mathcal{D}^M$, exists for both dynamos.

The mechanism for transforming TKE to TME differs between a large- and a small-scale turbulent dynamo, R10Pm0.1F, and R10Pm1F, with the large-scale production of TME ($\mathcal{P}_1$) playing a significant role in the former. The increasing energy in the large-scale magnetic field with increased magnetic diffusion is reflected by the large-scale magnetic field stretching term $\mathcal{P}_1$. However, the production of magnetic energy by small-scale magnetic field stretching $\mathcal{P}_3$ remains the dominant contributor to TME production for both dynamos. We note here that increasing magnetic diffusion in R10Pm0.1F gives rise to a wider range of energetic scales in the magnetic energy spectrum as compared with R10Pm1F. Therefore, the mechanism of large-scale magnetic field generation with increased magnetic diffusivity should be useful for interpreting the large-scale field generation in astrophysical dynamos with a strongly turbulent velocity field.

In contrast to the large-scale dynamo R10Pm0.1F, the large-scale field-stretching, $\mathcal{P}_1$, becomes the dominant mechanism of TME production in the weakly nonlinear dynamo R2Pm0.2N. In this dynamo, production of MME from TKE occurs via the term $\mathcal{P}_2$ in the presence of a mean magnetic field gradient. For R2Pm0.2N, an upscale energy transfer takes place through $\mathcal{P}_6$, which produces MME at the expense of TME. However, the production rate of MME is found to be smaller compared with the rate of production of TME for all of the investigated cases. The large-scale dynamo R2Pm0.2N exhibits strong time variability, as reported in previous literature (Stellmach & Hansen 2004).

An obvious extension of our study would be an introduction of a large-scale mean shear similar to Hughes & Proctor (2009, 2013), where the MKE will play a significant role in the budget. Additionally, scaling of these energy budget terms in the limit of small viscous and

inertial forces, following Calkins *et al.* (2015), should provide valuable insights into the energy conversion mechanism in astrophysical dynamos. Finally, a shell-to-shell energy transfer analysis similar to Guzmán *et al.* (2020) may elucidate further details on the large-scale magnetic field generation mechanism.

Declaration of interests. The authors report no conflict of interest.

Author contributions. The authors contributed equally to analysing data and reaching conclusions and in writing the paper.

Appendix A.

To disentangle the effect of velocity and magnetic boundary conditions, the TKE budget terms in non-magnetic rotating convection simulations with no-slip (NS) and free-slip (FS) boundaries (figures 13*a* and 13*b*), are compared with dynamo simulations with no-slip and conducting (NSC), free-slip and conducting (FSC), no-slip and vertical (NSV), free-slip and vertical (FSV) boundary conditions for $\mathcal{R} = 10$ (figure 13*c–f*, respectively). Here, we have used simulation data from our earlier study (Naskar & Pal 2022*b*). The behaviour of TKE terms in non-magnetic rotating convection (figures 13*a* and 13*b*) are similar for left and right columns in this figure (i.e. while comparing no-slip and free-slip boundaries), indicating limited contribution of the velocity boundary layers in the energetics. However, while comparing the NSC and NSV cases (figures 13*c* and 13*e*), the amount of TKE converted to IE via viscous dissipation ($\mathcal{D}$) is higher than the production of magnetic energy ($\mathcal{P}$) for NSC, whereas the latter is higher for NSV. Similar alterations in the order of these terms can be found while comparing FSC and FSV cases (figures 13*d* and 13*f*). Therefore, magnetic boundary conditions appear to have more influence on the budget terms as compared with the velocity boundary conditions, for $\mathcal{R} = 10$.

The effect of velocity and magnetic boundary conditions on the various terms in the TKE budget equation has also been reported in our previous work (Naskar & Pal 2022*b*). The viscous dissipation term ($\mathcal{D}$) was found to be higher with no-slip boundaries, both in the bulk and near the boundaries, which was attributed to the effect of Ekman pumping. It was also noted that the magnetic energy production ($\mathcal{P}$) was higher for no-slip as compared with free-slip boundaries. The magnetic boundary condition changes the vertical distribution of the terms of the TKE, especially the magnetic energy production ($\mathcal{P}$). However, the volume-average values of the terms in the TKE budget were found to be more sensitive to velocity boundary conditions than magnetic boundary conditions. The velocity boundary conditions seem to influence the magnitude of the terms, with higher values for no-slip as compared with free-slip conditions, whereas, the magnetic boundary conditions primarily modify their vertical distribution. However, the thermal forcing may influence the role of boundary conditions as Ekman pumping is not effective for high thermal forcing ($\mathcal{R} \geqslant 5$, see Naskar & Pal (2022*b*)) and the root-mean-square magnetic field strength increases with forcing. Therefore, at high thermal forcing ($\mathcal{R} = 10$, as shown in figure 13), the magnetic boundary conditions strongly influence the volume-averaged magnitude of the terms apart from the vertical profile. Therefore, the relative influence of velocity and magnetic boundary conditions seem to depend on $\mathcal{R}$. In § 2.2.1, we demonstrate that the boundary conditions may influence the energy budgets. Here, we illustrate the individual effects of velocity and magnetic boundary conditions.
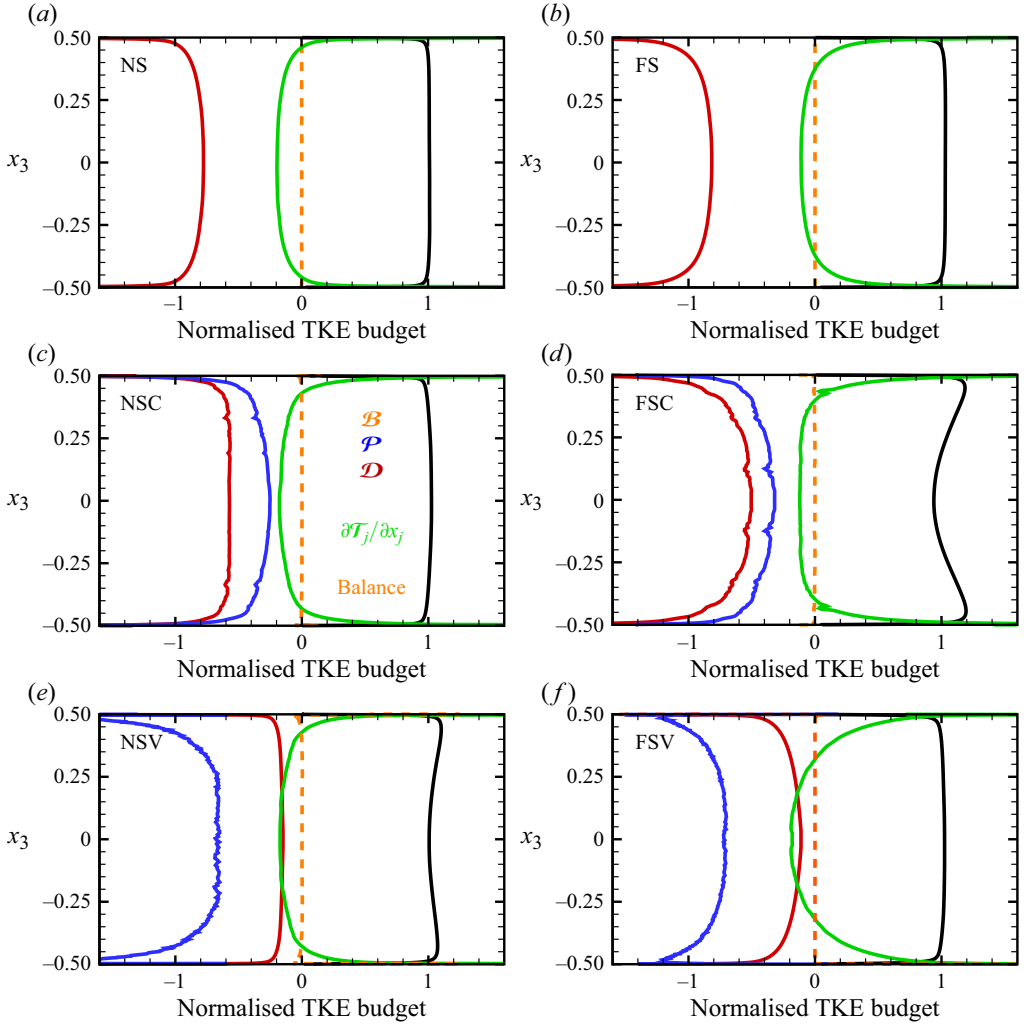
Figure 13. Vertical variation of TKE budget terms at $\mathcal{R} = 10$ for both no-slip (a, c, e) and free-slip (b, d, f) boundaries. Energy budget terms are presented for non-magnetic simulations (a, b) as well as dynamo simulations with both perfectly conducting (c, d) and pseudo-vacuum (e, f) conditions. The horizontally averaged budget terms in the TKE budget equation are averaged in time. The balance term (orange dashed line) signifies the difference between the left- and right-hand sides of the TKE budget equation and indicates sufficient accuracy of the present calculations.

We have also found large scale vortices (LSV) in the case R10Pm0.1F, in the present dynamo simulations, as expected in this parameter regime (Guervilly *et al.* 2015, 2017). However, in this case, the LSV is not energetically dominant, with a total to vertical kinetic energy ratio of 1.84, which is much lower than the value for the corresponding non-magnetic case (7.76) with a strong LSV (Naskar & Pal 2022b). This case is similar to some of the cases reported by Bushby *et al.* (2018) and Yan & Calkins (2022b), where energetically weak LSVs have been reported. Therefore, a more systematic study with varied Ra and Pm would be needed in the future to draw any general conclusion about the importance of LSVs in our simulations.

Journal of Fluid Mechanics

REFERENCES

BAKHUIS, D., OSTILLA-MÓNICO, R., VAN DER POEL, E.P., ERWIN, P., VERZICCO, R. & LOHSE, D. 2018 Mixed insulating and conducting thermal boundary conditions in Rayleigh–Bénard convection. *J. Fluid Mech.* **835**, 491–511.

BRACKBILL, J.U. & BARNES, D.C. 1980 The effect of nonzero $\nabla \cdot B$ on the numerical solution of the magnetohydrodynamic equations. *J. Comput. Phys.* **35**, 426–430.

BRANDENBURG, A., JENNINGS, R.L., NORDLUND, Å., RIEUTORD, M., STEIN, R.F. & TUOMINEN, I. 1996 Magnetic structures in a dynamo simulation. *J. Fluid Mech.* **306**, 325–352.

BRANDENBURG, A. & SUBRAMANIAN, K. 2005 Astrophysical magnetic fields and nonlinear dynamo theory. *Phys. Rep.* **417** (1-4), 1–209.

BRUCKER, K.A. & SARKAR, S. 2010 A comparative study of self-propelled and towed wakes in a stratified fluid. *J. Fluid Mech.* **652**, 373–404.

BUSHBY, P.J., KÄPYLÄ, P.J., MASADA, Y., BRANDENBURG, A., FAVIER, B., GUERVILLY, C. & KÄPYLÄ, M.J. 2018 Large-scale dynamos in rapidly rotating plane layer convection. *Astron. Astrophys.* **612**, A97.

CALKINS, M.A. 2018 Quasi-geostrophic dynamo theory. *Phys. Earth Planet. Inter.* **276**, 182–189.

CALKINS, M.A., JULIEN, K., TOBIAS, S.M. & AURNOU, J.M. 2015 A multiscale dynamo model driven by quasi-geostrophic convection. *J. Fluid Mech.* **780**, 143–166.

CATTANEO, F. & HUGHES, D.W. 2006 Dynamo action in a rotating convective layer. *J. Fluid Mech.* **553**, 401–418.

CHANDRASEKHAR, S. 1961 *Hydrodynamic and Hydromagnetic Stability*. Courier Corporation.

CHILDRESS, S. & SOWARD, A.M. 1972 Convection-driven hydromagnetic dynamo. *Phys. Rev. Lett.* **29** (13), 837–839.

FAUTRELLE, Y. & CHILDRESS, S. 1982 Convective dynamos with intermediate and strong fields. *Geophys. Astrophys. Fluid Dyn.* **22** (3-4), 235–279.

FAVIER, B. & BUSHBY, P.J. 2013 On the problem of large-scale magnetic field generation in rotating compressible convection. *J. Fluid Mech.* **723**, 529–555.

FAVIER, B., SILVERS, L.J. & PROCTOR, M.R.E. 2014 Inverse cascade and symmetry breaking in rapidly rotating Boussinesq convection. *Phys. Fluids* **26** (9), 096605.

GAYEN, B., HUGHES, G.O. & GRIFFITHS, R.W. 2013 Completing the mechanical energy pathways in turbulent Rayleigh–Bénard convection. *Phys. Rev. Lett.* **111** (12), 124301.

GUERVILLY, C., HUGHES, D.W. & JONES, C.A. 2014 Large-scale vortices in rapidly rotating Rayleigh–Bénard convection. *J. Fluid Mech.* **758**, 407–435.

GUERVILLY, C., HUGHES, D.W. & JONES, C.A. 2015 Generation of magnetic fields by large-scale vortices in rotating convection. *Phys. Rev. E* **91** (4), 041001.

GUERVILLY, C., HUGHES, D.W. & JONES, C.A. 2017 Large-scale-vortex dynamos in planar rotating convection. *J. Fluid Mech.* **815**, 333–360.

GUZMÁN, A.J.A., MADONIA, M., CHENG, J.S., OSTILLA-MÓNICO, R., CLERCX, H.J.H. & KUNNEN, R.P.J. 2020 Competition between ekman plumes and vortex condensates in rapidly rotating thermal convection. *Phys. Rev. Lett.* **125** (21), 214501.

HUGHES, D.W. 2018 Mean field electrodynamics: triumphs and tribulations. *J. Plasma Phys.* **84** (4), 735840407.

HUGHES, D.W. & PROCTOR, M.R.E. 2009 Large-scale dynamo action driven by velocity shear and rotating convection. *Phys. Rev. Lett.* **102** (4), 044501.

HUGHES, D.W. & PROCTOR, M.R.E. 2013 The effect of velocity shear on dynamo action due to rotating convection. *J. Fluid Mech.* **717**, 395–416.

KÄPYLÄ, P.J., KORPI, M.J. & BRANDENBURG, A. 2009 Alpha effect and turbulent diffusion from convection. *Astron. Astrophys.* **500** (2), 633–646.

KERR, R.M. 2001 Energy budget in Rayleigh–Bénard convection. *Phys. Rev. Lett.* **87** (24), 244502–1–244502–4.

KUNNEN, R.P.J., GEURTS, B.J. & CLERCX, H.J.H. 2009 Turbulence statistics and energy budget in rotating Rayleigh–Bénard convection. *Eur. J. Mech. B Fluids* **28** (4), 578–589.

LUMLEY, L.J. & TENNEKES, H. 1997 *A Fisrt Course in Turbulence*. The MIT Press.

MENEGUZZI, M. & POUQUET, A. 1989 Turbulent dynamos driven by convection. *J. Fluid Mech.* **205**, 297–318.

MOFFATT, K. & DORMY, E. 2019 *Self-Exciting Fluid Dynamos*. Cambridge University Press.

NASKAR, S. & PAL, A. 2022*a* Direct numerical simulations of optimal thermal convection in rotating plane layer dynamos. *J. Fluid Mech.* **942**, A37.

NASKAR, S. & PAL, A. 2022*b* Effects of kinematic and magnetic boundary conditions on the dynamics of convection-driven plane layer dynamos. *J. Fluid Mech.* **951**, A7.

PAL, A. 2020 Deep learning emulation of subgrid-scale processes in turbulent shear flows. *Geophys. Res. Lett.* **47** (12), e2020GL087005.

PAL, A. & CHALAMALLA, V.K. 2020 Evolution of plumes and turbulent dynamics in deep-ocean convection. *J. Fluid Mech.* **889**, A35.

PAL, A. & SARKAR, S. 2015 Effect of external turbulence on the evolution of a wake in stratified and unstratified environments. *J. Fluid Mech.* **772**, 361–385.

PAL, A., DE STADLER, M.B. & SARKAR, S. 2013 The spatial evolution of fluctuations in a self-propelled wake compared to a patch of turbulence. *Phys. Fluids* **25** (9), 095106.

PETSCHEL, K., STELLMACH, S., WILCZEK, M., LÜLFF, J. & HANSEN, U. 2015 Kinetic energy transport in Rayleigh–Bénard convection. *J. Fluid Mech.* **773**, 395–417.

PHAM, H.T., SARKAR, S. & BRUCKER, K.A. 2009 Dynamics of a stratified shear layer above a region of uniform stratification. *J. Fluid Mech.* **630**, 191–223.

SINGH, N. & PAL, A. 2023 The onset and saturation of the faraday instability in miscible fluids in a rotating environment. *J. Fluid Mech.* **973**, A6.

SINGH, N. & PAL, A. 2024*a* Evolution of the rotating Rayleigh–Taylor instability under the influence of magnetic fields. arXiv preprint arXiv: 2406.00514.

SINGH, N. & PAL, A. 2024*b* Quantifying the turbulent mixing driven by the faraday instability in rotating miscible fluids. *Phys. Fluids* **36** (2), 024116.

SOWARD, A.M. 1974 A convection-driven dynamo i. the weak field case. *Phil. Trans. R. Soc. Lond. A* **275** (1256), 611–646.

STELLMACH, S. & HANSEN, U. 2004 Cartesian convection driven dynamos at low Ekman number. *Phys. Rev. E* **70** (5), 056312.

TILGNER, A. 2012 Transitions in rapidly rotating convection driven dynamos. *Phys. Rev. Lett.* **109** (24), 248501.

TOBIAS, S.M. 2021 The turbulent dynamo. *J. Fluid Mech.* **912**, P1.

VOGT, T., HORN, S. & AURNOU, J.M. 2021 Oscillatory thermal–inertial flows in liquid metal rotating convection. *J. Fluid Mech.* **911**, A5.

YAN, M. & CALKINS, M.A. 2022*a* Asymptotic behaviour of rotating convection-driven dynamos in the plane layer geometry. *J. Fluid Mech.* **951**, A24.

YAN, M. & CALKINS, M.A. 2022*b* Strong large scale magnetic fields in rotating convection-driven dynamos: the important role of magnetic diffusion. *Phys. Rev. Res.* **4** (1), L012026.